

Accepted Manuscript

Control of drop shape transformations in cooled emulsions

Diana Cholakova, Nikolai Denkov, Slavka Tcholakova, Ivan Lesov, Stoyan K. Smoukov

PII: S0001-8686(16)30079-3
DOI: doi: [10.1016/j.cis.2016.06.002](https://doi.org/10.1016/j.cis.2016.06.002)
Reference: CIS 1660

To appear in: *Advances in Colloid and Interface Science*



Please cite this article as: Cholakova Diana, Denkov Nikolai, Tcholakova Slavka, Lesov Ivan, Smoukov Stoyan K., Control of drop shape transformations in cooled emulsions, *Advances in Colloid and Interface Science* (2016), doi: [10.1016/j.cis.2016.06.002](https://doi.org/10.1016/j.cis.2016.06.002)

This is a PDF file of an unedited manuscript that has been accepted for publication. As a service to our customers we are providing this early version of the manuscript. The manuscript will undergo copyediting, typesetting, and review of the resulting proof before it is published in its final form. Please note that during the production process errors may be discovered which could affect the content, and all legal disclaimers that apply to the journal pertain.

Control of drop shape transformations in cooled emulsions

Diana Cholakova,¹ Nikolai Denkov,¹ Slavka Tcholakova,¹ Ivan Lesov,¹
Stoyan K. Smoukov*²

¹*Department of Chemical and Pharmaceutical Engineering*

Faculty of Chemistry and Pharmacy, Sofia University, Bulgaria

²*Active and Intelligent Materials Lab, Department of Materials Science & Metallurgy,
University of Cambridge, UK*

*Corresponding author:

Dr. Stoyan K. Smoukov

Department of Materials Science and Metallurgy

University of Cambridge

27 Charles Babbage Road,

Cambridge CB3 0FS

UK

E-mail: sks46@cam.ac.uk

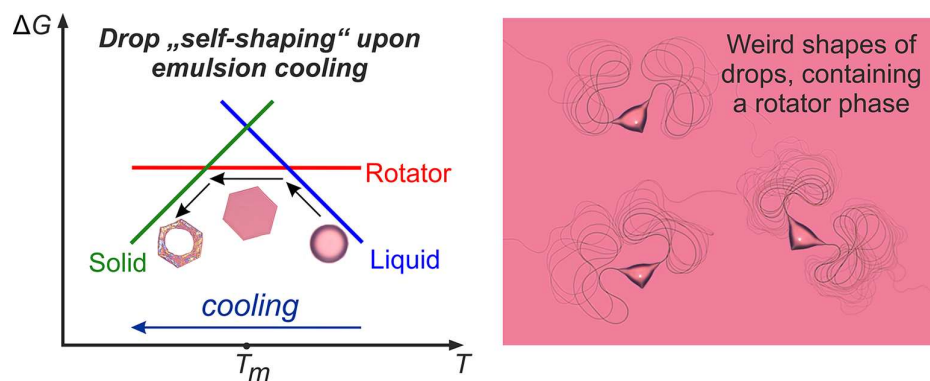
Tel: (01223) 334435

Fax (01223) 762088

Keywords: plastic crystal; rotator phase; emulsion; surface nucleation; self-shaping drops; tensegrity.

ABSTRACT

The general mechanisms of structure and form generation are the keys to understanding the fundamental processes of morphogenesis in living and non-living systems. In our recent study (Denkov et al., *Nature* 528 (2015) 392) we showed that micrometer sized *n*-alkane drops, dispersed in aqueous surfactant solutions, can break symmetry upon cooling and “self-shape” into a series of geometric shapes with complex internal structure. This phenomenon is important in two contexts, as it provides: (a) new, highly efficient bottom-up approach for producing particles with complex shapes, and (b) remarkably simple system, from the viewpoint of its chemical composition, which exhibits the basic processes of structure and shape transformations, reminiscent of morphogenesis events in living organisms. In the current study, we show for the first time that drops of other chemical substances, such as long-chain alcohols, triglycerides, alkyl cyclohexanes, and linear alkenes, can also evolve spontaneously into similar non-spherical shapes. We demonstrate that the main factors which control the drop “self-shaping”, are the surfactant type and chain length, cooling rate, and initial drop size. The studied surfactants are classified into four distinct groups, with respect to their effect on the “self-shaping” phenomenon. Coherent explanations of the main experimental trends are proposed. The obtained results open new prospects for fundamental and applied research in several fields, as they demonstrate that: (1) very simple chemical systems may show complex structure and shape shifts, similar to those observed in living organisms; (2) the molecular self-assembly in frustrated confinement may result in complex events, governed by the laws of elasto-capillarity and tensegrity; (3) the surfactant type and cooling rate could be used to obtain micro-particles with desired shapes and aspect ratios; (4) the systems studied serve as a powerful toolbox to investigate systematically these phenomena.

Graphical abstract

Contents

1. Introduction
2. Materials and methods
 - 2.1 Materials
 - 2.2 Emulsion preparation
 - 2.3 Optical observation of the drop shape transformations
 - 2.4 Interfacial tension
3. Experimental results
 - 3.1 General drop-shape evolution scheme
 - 3.2 Self-shaping for other hydrophobic phases
 - 3.3 Role of the difference between the chain-lengths of *n*-alkane and surfactant tail
 - 3.4 Effect of the cooling rate
 - 3.5 Effect of the initial drop size
 - 3.6 Effect of the surfactant head group
4. Discussion – mechanism of self-shaping
 - 4.1 Main processes driving the observed drop shape transformations
 - 4.2 Surface nucleation and rotator phases
 - 4.3 Explanations of the main observed trends
 - 4.4 Critical comparison of our experimental results with the explanation assuming ultra-low interfacial tension
5. Conclusions

Acknowledgements

References

1. Introduction

The general mechanisms of structure and form generation are the keys to understanding the fundamental process of morphogenesis in living and non-living systems [1-6]. The classical problem of crystal growth and shaping, studied in great details along the last century [7-10], is only a small subset of the mechanisms relevant to morphogenesis, structure formation, and control of crystal habits in the biological world [11-12]. In several remarkable examples, such as simple viruses and some bio-tissues (e.g., teeth enamel), true crystallization to minimum energy structures is a key step in the overall process of shape/structure formation [13-17]. However, in most cases the bio-composites (e.g. nacre) and structured biological materials (e.g. structural color, skin epidermis) rely on the formation, maintenance, and phase control of amorphous and partially ordered metastable phases - processes which lead to the rich variety of bio-structures we observe around us and allow the exhibition of different properties from chemically similar materials [18,19].

Turing's 1952 paper "The Chemical Basis of Morphogenesis" has established reaction-diffusion mechanisms as the paradigm of complex morphogenesis in biology [1]. The understanding of the biological mechanisms of morphogenesis has been greatly expanded in the last decades and several fundamentally new processes for morphogenesis in non-living systems were described as well [2,3]. Symmetry breaking from coupling growth and nonlinear deformation properties of materials was shown to be relevant to both biological [4] and non-biological systems [5,6]. These studies reveal that complex morphogenesis may combine a variety of mechanisms, some of them involving molecular and cellular transport and reactions, while others involving the development of mechanical stresses and non-symmetrical deformations.

Therefore, there is a need to define new experimental systems, which are as simple as possible with respect to their chemical composition, while still exhibiting the basic processes of morphogenesis in the living and non-living world. Such systems could serve as indispensable toolboxes for in-depth investigation of the main phenomena and the underlying mechanisms in morphogenesis.

In addition to the fundamental interest in the process of morphogenesis, there is a practical motivation to create different shapes. Particle shape is a key attribute, defining many properties of the biological and non-biological dispersions of particles. For example, particle shapes control the phenomena of colloidal aggregation [20], close-packing and formation of hierarchical structures [21], and affect strongly the macroscopic flow properties of particulate dispersions, such as the rheological characteristics, dispersion jamming and shear-banding [22,23].

Two main approaches are widely used to control particle shape and new ones are under development. The first "classical" approach relies on selective adsorption of surfactants on the faces of growing crystals and modification of their surface energy – faces with lower energy have a preference for faster area increase [24,25]. Micro and nano particles with cubic, pyramidal, spherical, ellipsoidal, rod-like, platelet-like and other shapes are synthesized by this approach [24-27]. More complex shapes are obtained by using nucleation seeds, and inducing growth of several crystals from one region [28].

The second, more recent approach starts with liquid droplets which are forced to acquire a given shape in an external field and afterwards are solidified to fix this shape [29-32]. Predominantly spherical (e.g. latex particles, formed under the action of the capillary pressure), elongated or fibrous solid particles were synthesized in this way. The control over size and shape in this approach is more independent of the molecular composition and interactions, but the variety of possible shapes is limited and regular geometric shapes with sharp corners are hard to achieve.

The last decade has seen a rapidly growing interest in synthesizing colloid particles with more sophisticated shapes and structures (e.g., bi-polar Janus particles, tetrahedral complexes, etc.), which could be used for assembly of complex hierarchical structures [33-36]. There have been a number of reports that combine physical confinement with directed growth, which have achieved a larger variety of shapes. These include electrical field phase switching of confined liquid crystal droplets [37], confinement of particles in droplets to generate directional clusters and patchy particles [38,39], oriented attachment methods where mesocrystals can grow in highly parallel ways to create various shapes [40,41], and controlled coalescence of particle-stabilized droplets to generate non-spherical liquid shapes [42].

Recently, we reported [43] a novel bottom-up mechanism for morphogenesis within droplets of linear alkanes, which leads to the formation of micrometer sized particles with different shapes. This phenomenon is driven by the formation of a “skin” of intermediate rotator phases in cooled alkane droplets – a process which was triggered by freezing adsorption layers of long-chain surfactants. These rotator phases (called also “plastic crystals” or “highly ordered smectics”) are characterized with a long-range translational order of the molecules, yet with some rotational freedom around the long molecular axis in the case of linear alkanes [44]. We showed [43] how the formation of anisotropic rotator phases, within the confines of the micro-scale fluid droplets, results in a surprisingly wide array of regular geometric shapes, including regular polyhedra; hexagonal, tetragonal and trigonal platelets, with and without fibers protruding from their corners. Furthermore, we found that frozen solid particles with the respective shapes can be produced by selecting appropriate cooling rates.

In this way, we succeeded in making a non-trivial link between a novel process for making complex shapes in materials science and the fundamental discovery that phase transitions confined inside a drop could be a driving force for morphogenesis [43]. The process opens new opportunities for both scalable particle synthesis and studying the structure/shape formation processes in amazingly simple chemical systems.

In the current study we describe and explain the main factors which can be used to push this process of drop “self-shaping” into desired directions. First, we demonstrate that drops of other substances, such as long-chain alcohols, triglycerides, alkyl cyclohexanes, and linear 1-alkenes, can evolve into similar non-spherical shapes. These new results show that the observed phenomenon is not very specific to the molecular structure of the oil in the droplet or surfactant on the surface and could open the door for a range of new studies in the areas of particle synthesis and morphogenesis mechanisms. Second, we classify the surfactants studied into four categories with respect to their effect on the “self-shaping” phenomenon. Third, we show that the evolution of high aspect ratio

shapes includes a specific transition, in which a capillary instability leads to formation of very long, sub-micrometer in diameter fibers. The latter observation is explained with the appearance of two rotator phases along the cooling process. Coherent explanations of the main experimental trends are proposed.

2. Materials and methods.

2.1. Materials.

For the dispersed phase in most experiments we used linear hydrocarbons (*n*-alkanes), with chain-lengths between 14 and 20 carbon atoms (C-atoms). These alkanes have the melting point of their bulk phase, T_m , in the range between 6 °C and 37 °C. Detailed information for the chemical purity, physical properties and producers of the alkanes used is presented in Supporting Information **Table S1**. The main physical characteristics of all these alkanes, relevant to the current study, show only minor variation in the following ranges: mass density, $\rho = 758$ to 776 kg/m³, specific heat capacity, $C_p = 438$ to 641 J/mol.K, thermal conductivity, $\kappa = 0.141$ to 0.149 W/m.K, and thermal diffusivity, $\chi = 8.1 \times 10^{-8}$ to 8.5×10^{-8} m²/s. The hexadecane was further purified from its as-received state, to remove potential surface-active contaminations before using it, by passing through a glass column filled with Florisil adsorbent. The other alkanes were used as received.

As the dispersed phase in a separate series of experiments we used the following organic substances: 1-alcohols with 10, 12 and 14 carbon atoms (1-decanol, 1-dodecanol and 1-tetradecanol); 1,2,3-triacylglycerides with 12, 14 and 16 carbon atoms in the fatty chains (trilaurin, trimyristin and tripalmitin); pentadecylcyclohexane; 1-heptadecene and 1-eicosene. The chemical structures of these substances are described in **Table 1**, while their producers and main properties are presented in **Table 2**.

As emulsifiers we used a wide range of water soluble surfactants: the nonionic surfactants polyoxyethylene alkyl ethers (C_nEO_m) and polyoxyethylene sorbitan monoalkylates ($C_nSorbEO_{20}$) with n varied between 12 and 40, and m varied between 2 and 50; anionic surfactants sodium alkyl sulfates (C_nSO_4Na) with n varied between 12 and 18; and the cationic surfactant cetyltrimethyl ammonium bromide (CTAB). Detailed information for the purity, HLB values of the nonionic surfactants and surfactant producers is presented in **Table 3**. All emulsifiers were used without further purification. Their concentration in the aqueous phase was fixed at 1.5 wt % for all nonionic surfactants, and at 0.37 wt % for the ionic ones. These concentrations were chosen to be sufficiently high, well above the critical micelle concentrations of the respective surfactants, to suppress the possible drop-drop coalescence and surfactant depletion (due to adsorption on the increased surface of the deformed drops) during the experiments.

All aqueous solutions were prepared with deionized water, which was purified by an Elix 3 module (Millipore).

Table 1. Structural formulas of the non-alkane organic phases studied.

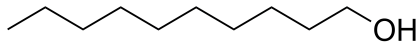
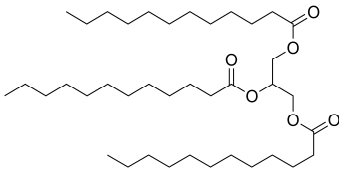
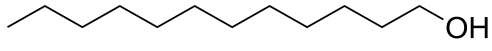
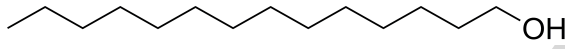
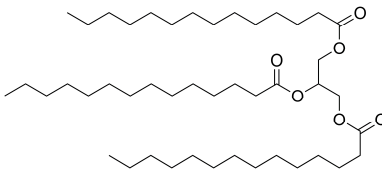
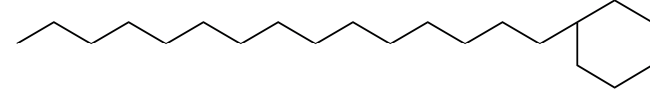
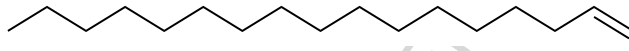
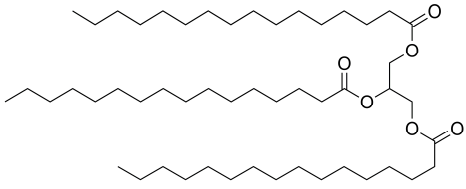
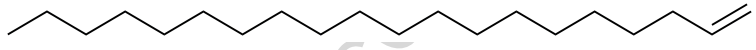
Chemical name	Structural formula	Chemical name	Structural formula
1-decanol		1,2,3 – tridodecylglyceride (trilaurin)	
1-dodecanol			
1-tetradecanol		1,2,3 – tritetradecylglyceride (trimyristin)	
Pentadecylcyclohexane			
1-heptadecene		1,2,3 – trihexadecylglyceride (tripalmitin)	
1-eicosene			

Table 2. Properties of the non-alkane organic phases studied (hexadecane is presented for comparison).

	Chemical formula	Molecular weight, Mw, g/mol	Producer	Purity	Melting point, T _m , °C	Mass density, ρ, kg/m ³	Specific heat capacity, C _p , J/mol.K	Thermal conductivity, κ, W/m.K	Thermal diffusivity, χ, m ² /s
<i>n</i> -hexadecane [45]	C ₁₆ H ₃₄	226.4	Sigma Aldrich	> 99%	18	763 (36°C)	507	0.144	8.4×10 ⁻⁸
1-decanol [45]	C ₁₀ H ₂₁ OH	158.3	Aldrich	99%	6.6	826 (25°C)	374	0.164	8.4×10 ⁻⁸
1-dodecanol [45]	C ₁₂ H ₂₅ OH	186.3	Sigma	99%	24	822 (36°C)	453	0.168	8.4×10 ⁻⁸
1-tetradecanol [45]	C ₁₄ H ₂₉ OH	214.4	Merck	> 98%	36-39	817 (48°C)	530	0.169	8.4×10 ⁻⁸
1-heptadecene [45]	C ₁₇ H ₃₄	238.5	TCI Chemicals	> 99.5%	11-11.5	783 (25°C)	513	0.150	8.9×10 ⁻⁸
1-Eicosene [45]	C ₂₀ H ₄₀	280.5	TCI Chemicals	> 97%	28.5-29	815 (36°C)	618	0.153	8.5×10 ⁻⁸
1,2,3-tridodecylglyceride (trilaurin)	C ₃₉ H ₇₄ O ₆	639.0	Alfa Aesar	≥ 99%	46.3	902 (50°C) [45]	1305 [45]	0.168 [46]	9.1×10 ⁻⁸
1,2,3-tritetradecylglyceride (trimyristin)	C ₄₅ H ₈₆ O ₆	723.2	Sigma Aldrich	≥ 99%	57	872 (60°C) [45]	1500 [45]	0.166 [46]	9.2×10 ⁻⁸
1,2,3-trihexadecylglyceride (tripalmitin)	C ₅₁ H ₉₈ O ₆	807.3	TCI Chemicals	99%	65.7	874 (70°C) [45]	1674 [45]	0.164 [46]	9.0×10 ⁻⁸
Pentadecylcyclohexane [45]	C ₂₁ H ₄₂	294.6	TCI Chemicals	≥ 98%	29	823 (30°C)	678	0.157	8.3×10 ⁻⁸

2.2. Emulsion preparation.

All emulsions were prepared by membrane emulsification, in which drops with a relatively narrow size distribution were generated [47,48]. The non-polar (oily) phase was emulsified by passing it through the membrane pores under pressure, into the continuous phase (aqueous surfactant solution). We used a laboratory Microkit membrane emulsification module from Shirasu Porous Glass Technology (SPG, Miyazaki, Japan), working with tubular glass membranes of outer diameter 10 mm and working area of approx. 3 cm². Membranes with mean pore diameter of 2 μm, 3 μm, 5 μm or 10 μm were used for preparing emulsions with different drop diameters. Typically, drops with diameter around 3 times bigger than the pore diameter are produced by this method [47]. When preparing emulsions with substances which are solid at room temperature, we melt them by heating before emulsification and maintain sufficiently high temperature in the laboratory to avoid a liquid-solid phase transition during emulsification.

2.3. Optical observation of the drop shape transformations.

The emulsions, prepared as described in Section 2.2, were transferred into glass capillaries with rectangular cross-section: 50 mm length, 1 mm width and 0.1 mm height, enclosed within a custom-made cooling chamber, with optical windows for microscope observation, see **Figure 1**.

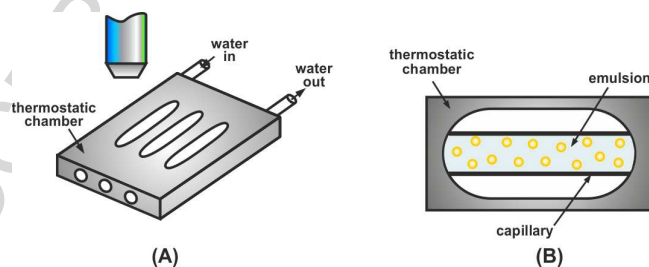


Figure 1. (A) Schematic presentation of the cooling chamber, made of aluminum, with cut optical windows, used for microscope observation of the emulsion samples. (B) The emulsions studied were contained in glass capillaries with rectangular cross-section, placed in the thermostatic chamber and observed through the optical windows [43].

The observations were performed with an optical microscope Axioplan or AxioImager.M2m (Zeiss, Germany) in transmitted, cross-polarized white light. Long-focus $\times 20$, $\times 50$ or $\times 100$ objectives, combined with built-in cross-polarizing accessories of the microscope, were used to observe the drops upon sample cooling. In most of the experiments we used an additional λ plate (compensator plate) which was situated between the polarizer and the analyzer, the latter two being oriented at 90° with respect to each other. The λ plate was oriented at 45° with respect to both the polarizer and the analyzer. Under these conditions the liquid background and the fluid objects have

a typical magenta color, whereas the birefringent areas appear brighter and may have intense colors [49,50].

The temperature of the cooling chamber was controlled by cryo-thermostat (Julabo CF30) and measured close to the emulsion location using a calibrated thermo-couple probe, with an accuracy of ± 0.2 °C. Experiments were carried out at different cooling rates, varied within two orders of magnitude – from 0.03 K/min to 2 K/min.

To quantify the drop deformation along the cooling process, we used the drop aspect ratio, defined as follows. As a reference drop size we used the diameter of the initial spherical drop. After the occurrence of drop shape transformations, we measured the longest length of the observed two-dimensional (2D) projection of the drop, see **Figure 2** for illustration. Typically, we followed the shape evolution of 5 to 10 drops in a given experiment. For each drop we made multiple measurements in consecutive moments along the shape transformation path. Thus we accumulated statistically relevant information about the aspect ratio of the deformed drops, defined as the ratio between the drop length in any moment of the experiment and the initial drop diameter. Moment $t = 0$ in all graphs below is the moment at which the first drop shape transformation is detected. The last point of each curve (shown with bigger symbols on the graphs) represents the drop deformation in the moment just before drop freezing into the final solid particle.

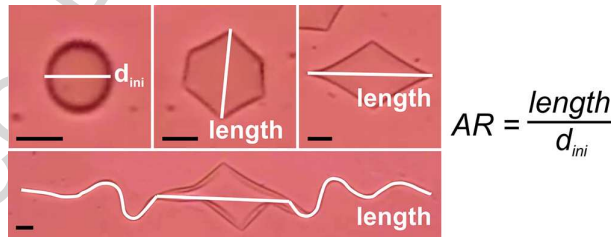


Figure 2. Sample images, used in the study of the kinetics of drop shape evolution. The white lines or curves represent the measured “length” of the drop in a given moment of the experiment. As a measure of drop deformation, we use the aspect ratio $AR = \text{length}/d_{ini}$. Scale bars, 20 μm .

Theoretical estimates of the time, τ , required to cool the center of an emulsion drop with diameter $d \approx 40$ μm to 95% of a temperature difference induced at its surface, assuming negligible drop heating due to phase transitions or to viscous friction inside the drop (both processes generate heat), indicate that this time is around 5 ms [51]:

$$\tau \approx \frac{d^2}{4\chi} = \frac{(40 \times 10^{-6})^2}{3.2 \times 10^{-7}} = 5 \times 10^{-3} \text{ s}$$

Here χ is the thermal diffusivity of the dispersed phase. Due to the low cooling rates in our experiments, we assume that the temperatures of the droplets and of the continuous phase were virtually the same. This assumption does not imply that all observed phenomena are equilibrium ones, as some of the drop shape transformations could take a very long time (e.g., the extrusion of the thin threads from the corners of the deformed drop).

Note that only the dispersed phase underwent phase transitions during our experiments and solidified at the end. The continuous medium (aqueous surfactant solution) always remained liquid.

2.4. Interfacial tension.

The hydrocarbon-water interfacial tension, γ , was measured by drop-shape analysis at different temperatures [52]. The shape of millimeter sized pendant oil drops, immersed in the surfactant solution, was recorded and analyzed by the Laplace equation of capillarity to determine the oil-water interfacial tension (instrument DSA100 by Krüss, Germany). The thermostating cell TC40 was used to vary the temperature of the measured system with a precision of $\pm 0.5^\circ\text{C}$. For the liquid alkanes, for all surfactant solutions studied, γ was measured to be in the range between 2 and 10 mN/m in the entire range from room temperature down to the temperatures of the observed pendant drop freezing.

3. Experimental results.

In the current section we present the main results, obtained with different combinations of surfactants and organic phases. As a reference and basis for discussion, we describe in Section 3.1 the main evolution scheme of the deforming droplets, as observed with n -alkanes. In Section 3.2 we demonstrate that similar phenomena could be observed with other organic substances. In Sections 3.3 to 3.5, we describe the effects of surfactant and n -alkane chain-lengths, cooling rate and drop size. In Section 3.6 we consider the subtler effects of the surfactant head-groups. The unified explanation of all these observations is presented in Section 4.

3.1 General drop-shape evolution scheme

We illustrate the general drop-shape evolution scheme with results obtained upon cooling of hexadecane emulsion drops, dispersed in aqueous solution of the nonionic surfactant $\text{C}_{16}\text{EO}_{20}$. The following series of transformations is observed (see **Figure 3**, **Video 1** and **Video 2**):

When the sample reaches some specific temperature range which depends on the alkane and surfactant used, spontaneously, shape changes appear in the initially spherical drop. For hexadecane drops stabilized by $C_{16}EO_{20}$ this temperature is $T_d \approx 11^\circ\text{C}$, well below the melting temperature of bulk hexadecane, $T_m \approx 18^\circ\text{C}$. For many of the other surfactants studied, however, the drop shape transformations started at temperatures which were close to or even higher (up to 23°C) than T_m . Note that the phenomenon of surface freezing for linear alkanes, at higher temperatures than the melting/freezing temperature of the bulk alkane, has been reported before [53,54]. Therefore, it is not surprising that the drop shape transformations could start at temperatures which are several degrees higher than T_m .

The overall sequence of shape transformations proceeds as follows. First, several vertices (convex tips) are seen to appear simultaneously on the drop surface, and the drop projection area soon acquires the shape of a hexagon. These observations indicate the formation of polyhedrons, e.g. icosahedrons or octahedrons (regular bodies enclosed by triangular faces) [43,55]. Three bright and three dark spots are alternatively seen, next to the vertexes of the observed hexagon. These spots of different brightness indicate that three of the vertexes are close to the wall of the glass capillary, to which the drop is attached under buoyancy, whereas the other three vertexes are situated in a lower plane, on the other side of the polyhedron.

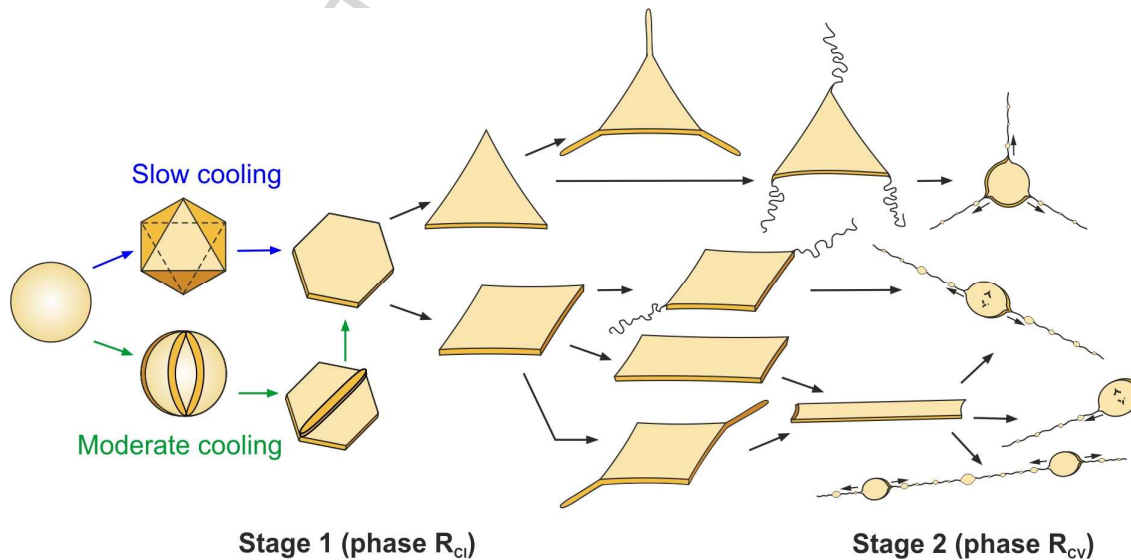


Figure 3. General evolution scheme for the drop-shape transformations upon cooling of micrometer sized hydrocarbon drops, dispersed in surfactant solutions, as observed with linear alkanes. The scheme is adapted from ref. [43] and expanded by including new information from the current study. Rotator phase R_{CI} forms on the edges of the geometric shapes in the first stage of the evolution. In the second stage, rotator phase R_{CV} forms very thin (sub-micron) fibres from the corners of larger structures, see text for further explanations.

With time, the polyhedron gradually flattens, forming a flat hexagonal prism (hexagonal platelet). Under the microscope, this process appears as the hexagon increases significantly its projected area and the bright and dark spots gradually disappear (merge with hexagon corners), thus indicating that all six vertices become very close to the same focal plane. For the larger drops and moderate cooling rates, this process might involve an intermediate stage in which the drop surface becomes strongly corrugated and the drop acquires the shape of a strongly deflated football balloon – see the lower branch in the transition “sphere \rightarrow hexagonal platelet” in **Figure 3** and **Video 3**. Afterwards, these corrugations gradually disappear and a flat hexagonal platelet is formed.

Upon further cooling, two (see **Video 1**) or three (see **Video 2**) of the hexagon sides disappear gradually, while the remaining four or three sides (respectively) elongate, thus forming a tetragonal or a triangular platelet. This process is statistical and depends on the cooling rate, drop size, surfactant type, and some other factors. Under all other conditions being equivalent, slower cooling of intermediate size droplets (10-20 μm in diameter) increases the probability for formation of triangular platelets, at the expense of the tetragonal ones.

Next, from the acute angles of the platelets rod-like asperities emerge (two from the tetragonal and three from the triangular platelets). The evolution of the triangles continues with the growing of rod-like asperities with diameter of $\approx 5 \mu\text{m}$ for hexadecane, until the drop finally freezes (for comparison, the asperity diameter is $\approx 3 \pm 1 \mu\text{m}$ for pentadecane and $\approx 1 \pm 0.5 \mu\text{m}$ for tetradecane, see **Video 2**). Alternatively, the tetragonal platelets may spontaneously elongate in one direction, while shrinking in the other, without growing rod-like asperities. When reaching a certain critical ratio between the length and the width of the expanding tetragonal platelets (about 22 ± 5 for C16/C₁₆EO₂₀), a capillary instability is observed (see **Video 1**) – a large fraction of the oil phase segregates into one or several ellipsoidal drops, from which several very thin fibers, with diameter $< 1 \mu\text{m}$, continue to protrude. The extrusion of these very thin fibers from the ellipsoidal drops may continue for many minutes, with fibers connecting all ellipsoidal droplets formed from an initial “mother” drop. The evidence that there is no fibre breakage and complete drop detachment is that all these ellipsoidal drops merge back into their original “mother” drop, if they are heated before the complete freezing of the drop material.

For a given system and cooling protocol, the observed processes are highly reproducible. Depending on the cooling protocol and the other factors discussed below, the deformed drops could freeze in any of these deformed states, thus fixing their shape into frozen solid particles. Choosing different surfactants, one could observe different branches of the general evolutions scheme and different shapes before the complete drop freezing, see **Figure 4** for examples.

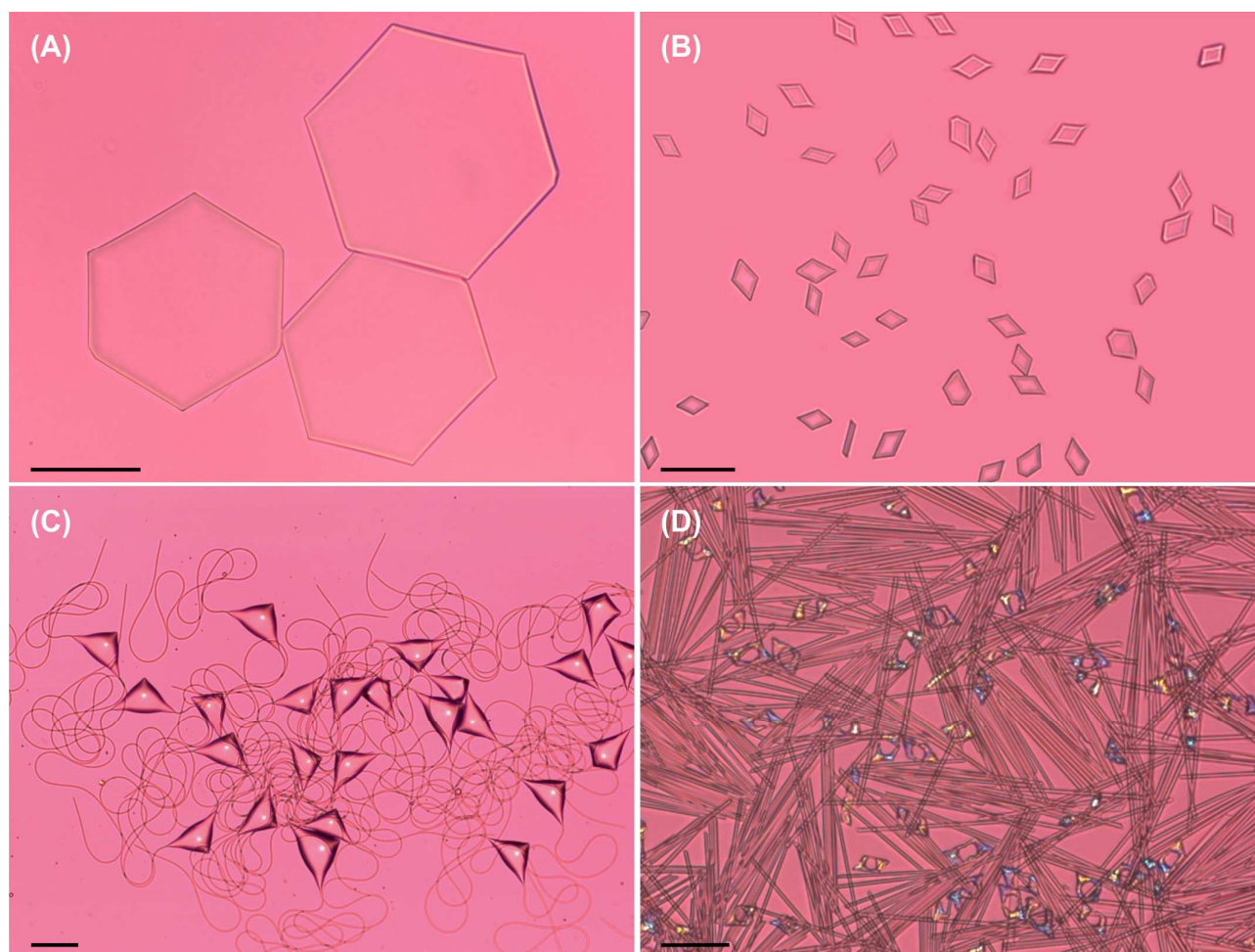


Figure 4. Images of ensembles of several drop shapes, captured along the evolution process shown in **Figure 3**. (A) Hexagonal platelets; (B) Parallelograms; (C) Bacteria-like droplets with long tails; (D) Fluid rods in coexistence with frozen parallelograms of toroidal topology. The drops in (A), (B) and (D) are from hexadecane, whereas the drops in (C) are from pentadecane. The surfactant used in (A) is $C_{16}\text{SorbEO}_{20}$, in (B) and (D) $C_{18}\text{SorbEO}_{20}$, and in (C) $C_{16}\text{EO}_{20}$. Scale bars, 50 μm .

3.2 Self-shaping for other hydrophobic phases

Similar drop shape evolution was also observed with other hydrophobic compounds, from molecular classes known to form rotatory plastic phases [56-61]. The chemical structures of the molecules which undergo similar drop-shape transitions are shown in **Table 1** and include three 1-alcohols with 10 to 14 carbon atoms, three triacylglycerides with 12 to 16 carbon atoms in the acyl chains, pentadecylcyclohexane, and two linear 1-alkenes with 17 and 20 carbon atoms, respectively. Images of deformed drops from these phases are shown in **Figure 5**. These images prove that the self-shaping phenomenon is relevant to a wide variety of compounds and is not limited to linear alkanes for which it was first reported [43].

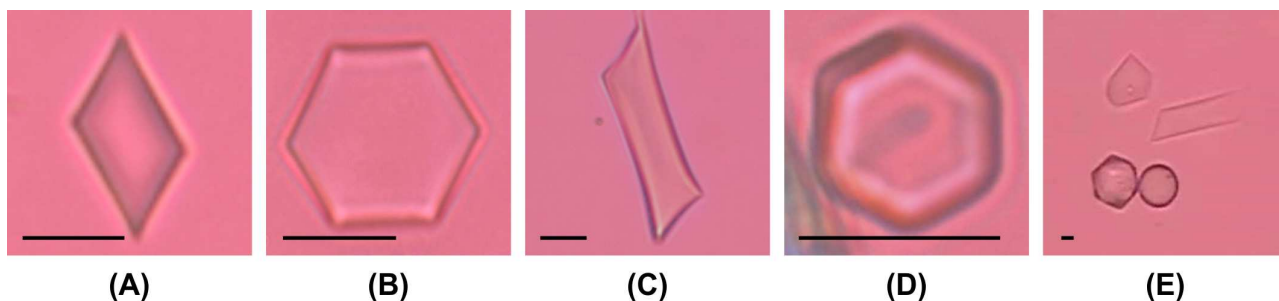


Figure 5. Panel of images of self-shaped deformed drops from organic liquids with different molecular structures. (A) 1-heptadecene; (B) 1-eicosene; (C) pentadecylcyclohexane; (D) tri-tetradecylglyceride; (E) 1-decanol. The drops from (A-D) are dispersed in solution of $C_{18}SorbEO_{20}$ nonionic surfactant, (E) in nonionic $C_{18}EO_{20}$. Scale bars, 10 μm .

Our experiments showed that the general evolution scheme and the main trends, reported for alkanes, were followed with all these other compounds. As in the case of alkanes, the drop-shape evolution is more pronounced for smaller drops, lower cooling rates, and larger difference between the lengths of the surfactant tail and oil/alkyl chain, see Sections 3.3-3.5 and 4.3 below. Specific deviations occur mostly in the onset temperature of drop deformation, the drop freezing temperature, and the final drop deformation in the moment of solidification. With some of these compounds, such as the triglycerides and alcohols, it was more difficult to induce shape transformations, compared to the linear alkanes – smaller droplets and lower cooling rates were needed, under otherwise equivalent conditions. With the others (the alkenes and the alkylcyclohexane) we did not observe a significant difference, as compared to linear alkanes, if appropriate surfactant and cooling rate are applied.

The fact that shelf-shaped drops are obtained with 1-decanol containing 10 carbon atoms, almost half the chain length of the $C_{18}EO_{20}$ surfactant used to stabilize the decanol drops, indicates that 1-decanol assembles in bilayers, as it was reported to be the case for alcohol rotator phases [56]. This explanation is confirmed by the fact that we needed surfactants with even longer tails of 22 carbon atoms to induce drop-shape transformations for the alcohols with 12 and 14 carbon atoms.

3.3. Role of the difference between the chain-lengths of *n*-alkane and surfactant tail.

In the following sections 3.3-3.6, we report results from the systematic series of experiments, performed with *n*-alkanes (tetradecane to eicosane), aimed to clarify the main factors controlling the drop “self-shaping” process.

When the alkane molecule is longer than the surfactant tail by more than three carbon atoms, the drops freeze in a spherical shape, regardless of the conditions used, see **Figure 6A**. Examples of this rule include systems with all types of surfactants, e.g. hexadecane (C16) drops, stabilized by C₁₂SorbEO₂₀, C₁₂EO₂₃ or C₁₂H₂₅SO₄Na surfactant. Drop-shape transformations were not observed either for any of the oils with C_{18d}SorbEO₂₀ surfactant (commercial name Tween 80) with a double bond in the middle of the surfactant tail. The double-bond kink seems to prevent ordering in the adsorption layer, even though the alkane is shorter. The drop freezing in these systems typically occurred in the range between 5 and 10 °C, well below the hexadecane melting temperature $T_m \approx 18$ °C. The latter “supercooling” effect is well known for emulsions and extensively studied in the literature [62-64]. It is due to the low probability for bulk nucleation in micrometer sized alkane droplets, due to their small volume, and is therefore used to study quantitatively the nucleation phenomena.

In contrast, the drop shape transformations in **Figure 3** were observed with all *n*-alkanes between 14 and 20 carbon atoms, when the emulsions were stabilized by surfactant with chain-length similar to or longer than the molecular length of the dispersed alkane (see **Figures 4, 6B, 6C** and **Figure 8 below**). The related phenomenon of surface nucleation by the freezing long chains of the surfactants in the adsorption layers, formed at the oil-water interface, is also well known in literature and widely studied [53,54]. However, the drop shape transformations (**Figure 3**) and their relation to the surface nucleation by surfactant adsorption layers were reported only last year [43].

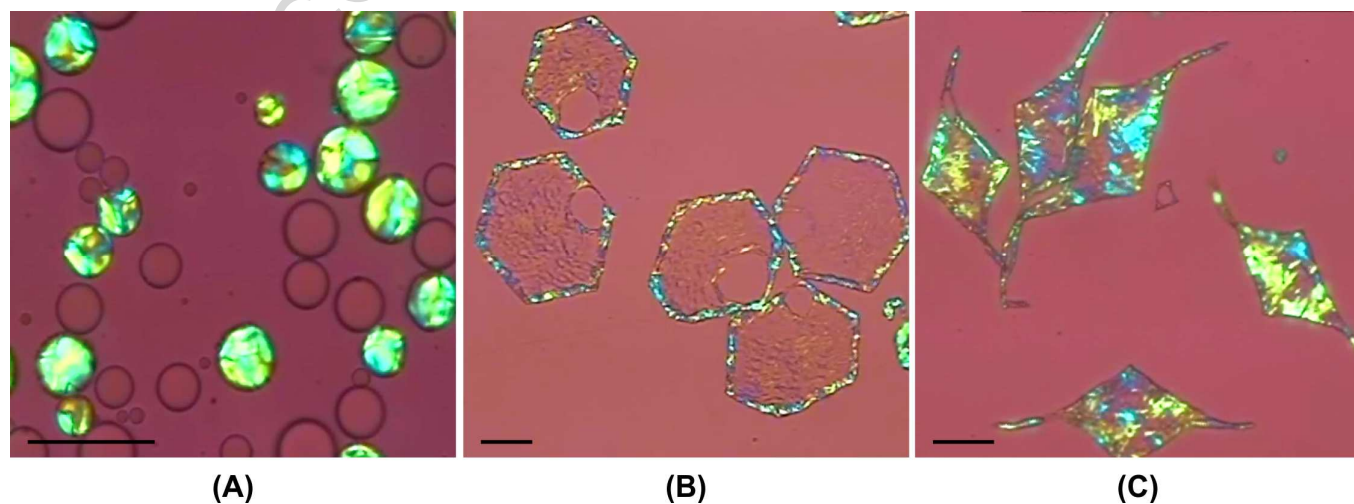


Figure 6. Pictures of solid particles obtained with different combinations of oils and surfactants: (A) C20/C₁₆EO₂₀, (B) C16/C₁₆SorbEO₂₀, (C) C16/C₁₆EO₂₀. Scale bars, 50 μ m.

When the same surfactant is used to stabilize emulsions of different *n*-alkanes, the droplets deform more before freezing, if a shorter alkane is used. This trend is illustrated in **Figure 7** with data for the evolution of C14, C16 and C17 droplets, stabilized by C₁₆EO₂₀ ($d_{ini} \approx 31\mu\text{m}$). One sees that the evolution of the three samples is rather different – C17 drops freeze soon after acquiring a polyhedral shape, at an aspect ratio $AR \approx 1.3 \pm 0.2$, whereas C16 drops evolve to elongated tetragonal platelets with $AR \approx 12 \pm 3$, **Figure 7B**. Under similar conditions, C14 drops evolve easily along the entire evolution scheme, cf. **Figures 3 and 7B**, reaching very large aspect ratios, $AR > 400$, due to the formation of long thin fibers. On the other end of the *n*-alkane molecular length, C20 drops do not deform at all before freezing with this surfactant (**Figure 6A**).

These and other experiments showed clearly that the chain-length difference between the linear alkanes in the droplets and the hydrocarbon surfactant tails in the adsorption layer is one of the key factors in the observed phenomena. The longer the surfactant tail in comparison to the alkane molecules, the more pronounced are the drop shape transformations observed. The initial drop size and the cooling rate turned out to be two other crucial factors – they are considered in the following two sections. The explanations of all these effects are presented in Section 4.

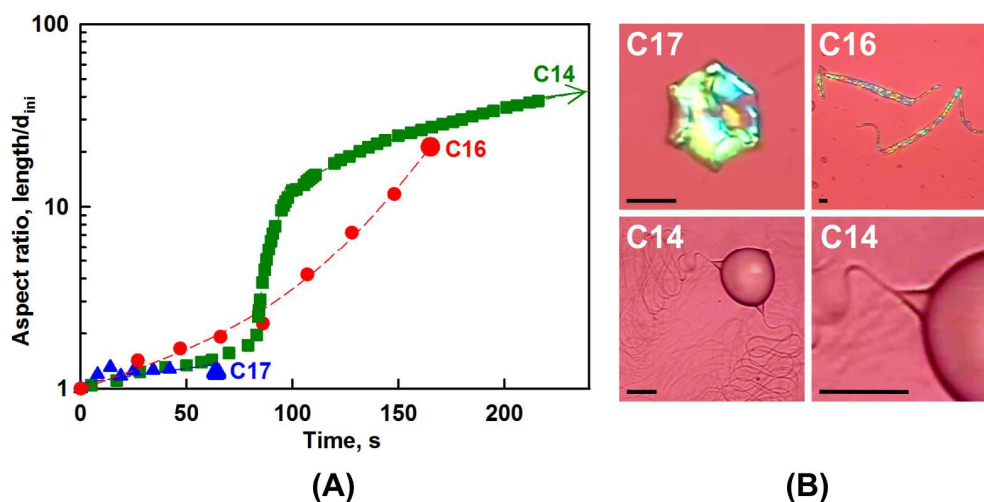


Figure 7. (A) Evolution of C14 (green squares), C16 (red circles) and C17 (blue triangles) drops with $d_{ini} \approx 31\mu\text{m}$ in C₁₆EO₂₀ solution, at a cooling rate of 0.43 K/min. (B) Pictures of frozen particles of C16 and C17, and two images (at lower and higher magnification, respectively) of a C14 drop, discharging thin long threads. Note the sharp conical tips on the drop surface from which the threads are extruded. Scale bars, 20 μm .

3.4 Effect of the cooling rate

Lower cooling rates favored droplets proceeding through shape transformations further along the evolution scheme in **Figure 3**, before they froze than at higher cooling rates. This effect is visualized in **Figure 8** with hexadecane droplets of $d_{\text{ini}} = 31 \pm 3 \mu\text{m}$, stabilized by $\text{C}_{16}\text{EO}_{20}$ surfactant. At a cooling rate of 1.4 K/min, all drops reach the stage of flat hexagonal platelets and then freeze, forming solid hexagonal platelets. When the cooling rate is below 1 K/min, tetragonal platelets are predominantly formed and rod-like asperities appear and grow from the platelet tips with acute angles ($\approx 60^\circ$), before the droplets freeze. At cooling rates lower than 0.5 K/min, the tetragonal platelets deform further and many of them reach the next stage of the evolutionary scheme, forming ellipsoidal drops which release thin fibers. At the lowest cooling rates studied ($< 0.2 \text{ K/min}$) all drops evolve to the final stages in the evolutionary scheme, forming either triangular platelets with rod-like asperities or ellipsoidal drops releasing thin fibers (**Figure 8**).

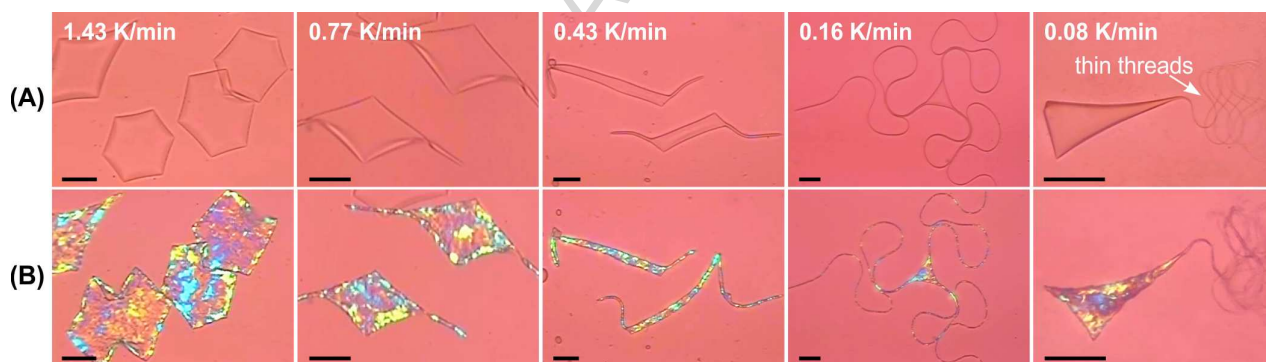


Figure 8. (A) Typical pictures from the moment just before final freezing of hexadecane droplets, stabilized with $\text{C}_{16}\text{EO}_{20}$ surfactant, for initial drop diameter, $d_{\text{ini}} \approx 31 \mu\text{m}$. The experiments are carried out at different cooling rates, as indicated on the pictures. (B) Pictures of the respective frozen particles, obtained from the droplets shown in (A). Scale bars, $50 \mu\text{m}$.

The drop evolution could be quantified by plotting the drop aspect ratio (AR) as a function of time, $AR(t)$, or temperature, $AR(T)$. Using such plots, in **Figure 9** we illustrate the effect of the cooling rate for the systems imaged in **Figure 8**. **Figure 9A** presents the drop length, as a function of time, for three cooling rates. The last (bigger) points in the respective curves indicate the moment just before drop freezing into the respective solid shape. One sees that the drops reach significantly larger lengths at lower cooling rates, before their freezing into solid particles. At a cooling rate of 0.16 K/min or lower, we obtain frozen particles with a total length of $\approx 2 \text{ mm}$, starting from a drop with an initial diameter of $\approx 31 \mu\text{m}$. This length corresponds to triangular platelets with very long rod-like protrusions. Even longer fibers, up to 6-9 mm in length, were detected in some of the systems at the final stage of the evolution process.

These results prove that the observed shape transformations are not caused by a temperature difference between the drops and the aqueous medium – otherwise, these transformations should be more pronounced at a higher cooling rate.

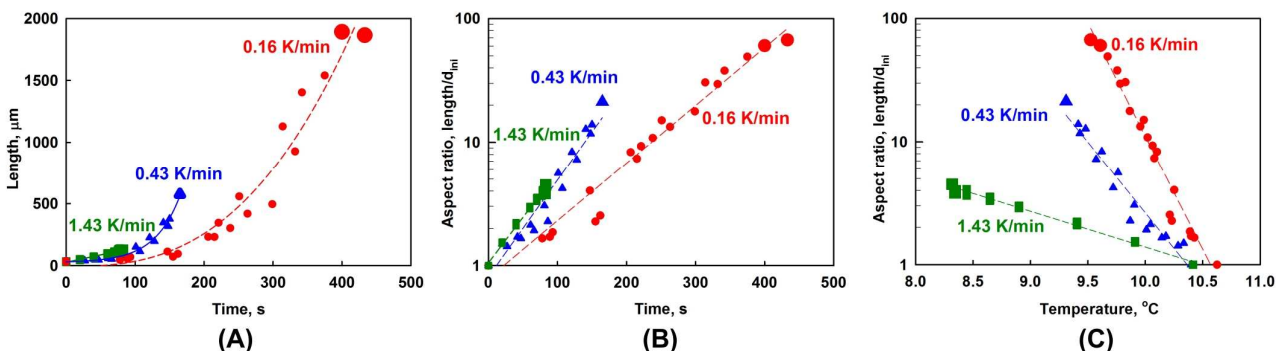


Figure 9. Evolution of the shape of C16 drops ($d_{ini} \approx 31 \mu\text{m}$) in aqueous solution of C₁₆EO₂₀. (A) Drop length, as a function of time of drop deformation. (B) Aspect ratio as a function of time. (C) Aspect ratio as a function of the sample temperature. Moment $t = 0$ corresponds to the first drop-shape transformation detected. The last (larger in size) points in the respective curves represent the drop deformation just before drop freezing.

Figure 9B presents the same experimental results, with the vertical axis being the aspect ratio of the droplets ($AR = \text{drop length} / \text{initial drop diameter}$), presented on a logarithmic scale. At high cooling rates, the droplets reach an aspect ratio of around 4-5 (platelets, see **Figure 8** for 1.44 K/min), while at slower cooling rates AR exceeds 80 (long fibers, see the data for 0.16 and 0.08 K/min in **Figure 8**).

Figure 9C shows the same data as a function of temperature. For this particular surfactant, C₁₆EO₂₀, the hexadecane drops start to deform when they are supercooled by 7-8 degrees below the melting point of the bulk hexadecane ($T_m \approx 18 \text{ }^\circ\text{C}$). Regardless of the cooling rate, the drop deformations start at approximately the same temperature, $T_d = 10.5 \pm 0.5 \text{ }^\circ\text{C}$). If the cooling rate is faster than the kinetics of the shape transformations, there is less time for the drops to evolve, though they reach lower temperatures before freezing. Reaching these lower temperatures leads to nucleation and arrest of the drop shapes in intermediate aspect ratios, due to drop solidification. In contrast, during slow cooling, the shape changes occur in a narrower temperature range of 1-2 degrees before the drops freeze completely, yet the droplets achieve shapes with much higher aspect ratios because of the additional time they have to evolve at these temperatures.

3.5 Effect of the initial drop size

To clarify the effect of drop size, several series of experiments were conducted with initial drop diameters varied between 2 and 100 μm .

When using low cooling rates (< 0.1 K/min) and appropriate surfactants with sufficiently long tails, we observed shape changes in drops within the entire studied drop size range. Droplets bigger than $100 \mu\text{m}$ were not studied, due to the limitation of our experimental set up – the height of the glass capillaries used is $100 \mu\text{m}$ and the larger drops would be deformed by the capillary walls. Such large drops would be deformed by gravity/buoyancy as well, thus compromising the experiment.

Remarkably, when the experiments were conducted with smaller drops (e.g., $d_{\text{ini}} < 15 \mu\text{m}$), we observed much easier drop shape evolution – all drops evolved to the last stages in the evolution scheme at low and moderate cooling rates. **Figure 10** illustrates the growth of aspect ratio with time for several diameters of hexadecane drops, stabilized by $\text{C}_{18}\text{SorbEO}_{20}$ surfactant. The initial part of the curves $AR(t)$ is virtually the same for all drops with different initial diameters. However, for the cooling rate of 0.44 K/min (**Figure 10A**) a significant difference in the curves is observed after the drops reach the platelet shape. The large drops ($d_{\text{ini}} > 15 \mu\text{m}$) freeze at this stage, at $AR \approx 4.5$, whereas the smaller droplets continue deforming to higher ratios. The cooling rate must be at least one order of magnitude lower for the largest drops to reach larger deformations. The smaller droplets reach a deformation of 30 ± 5 (the full symbols in the curves for 7 and $10 \mu\text{m}$ drops) when a capillary instability occurs and a fraction of the oil separates into one or several ellipsoidal drops, connected by thin filaments (the last evolution stage in **Figure 3**), resulting in the high aspect ratios (**Figure 10A**, empty symbols). These droplets continue to release thin fibers and the deformation increases. Because of the extensive fibers folding and the small fiber diameter ($0.7 \pm 0.2 \mu\text{m}$), a direct measurement of the fiber length is not possible. However, comparing the volume of the initial drop with that of the ellipsoidal drops and the diameter of the fibers formed, we estimated that the drop aspect ratio approaches 100 in this stage (the empty symbols for 7 and $10 \mu\text{m}$ drops in **Figure 10A**).

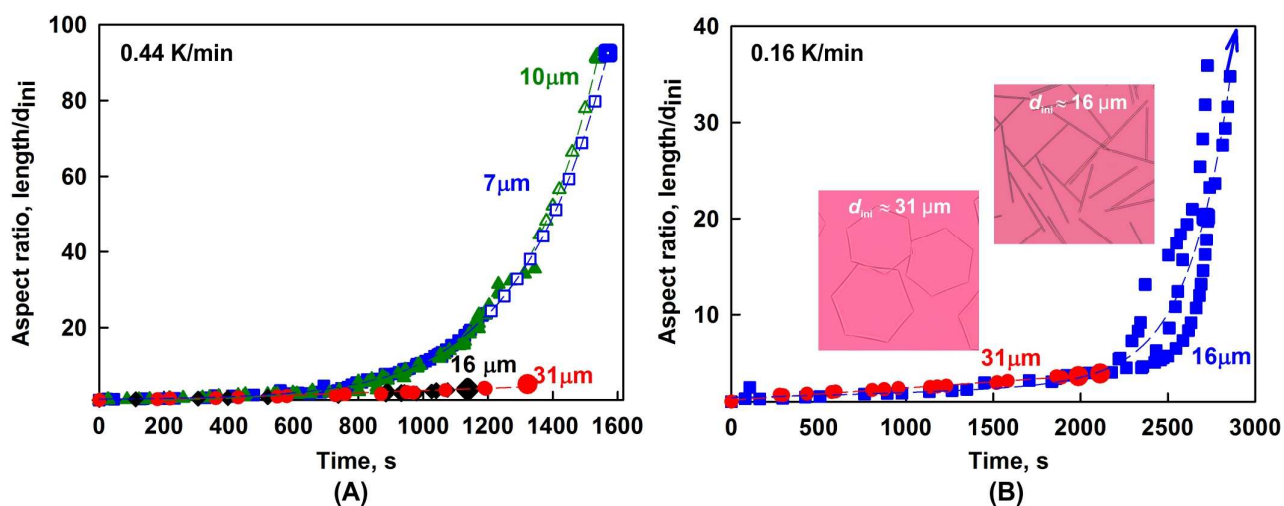


Figure 10. (A) Deformations of droplets of C16 in $\text{C}_{18}\text{SorbEO}_{20}$ solution, cooled at a cooling rate of 0.44 K/min. The drops have different initial drop size, as shown on the curves. (B) Deformations of C16 droplets in $\text{C}_{18}\text{SorbEO}_{20}$ solution, but at a cooling rate of 0.16 K/min. The inset microscope images show deformed drops of different initial diameter, d_{ini} .

These results illustrate the fact, found also in many other experiments from these series, that a threshold size exists for drops to deform at a given cooling rate. The bigger drops reach the platelet stage and freeze, whereas the smaller drops continue to deform into the later stages of the evolution scheme. For the system C16 in C₁₈SorbEO₂₀ and a cooling rate of 0.44 K/min, the threshold drop diameter to transform beyond platelets is around $13 \pm 3 \mu\text{m}$. Our experiments showed that the cooling rate must be lower than 0.2 K/min for drops with $d_{\text{ini}} = 16 \mu\text{m}$ to reach the next stages of the evolution scheme with formation of rods and fibers, see **Figure 10B**.

We conclude from all these experiments that a critical drop size and a critical cooling rate exist, associated with the transition from the stage of platelets ($AR \approx 4$) into the stage of elongated rods and thin fibers ($AR > 10$). Smaller droplets and lower cooling rates favor the transition into the final stages of highly deformed droplets, see Section 4 for further discussion of these trends.

3.6 Effect of the surfactant head group

Beside their chain length, surfactants are characterized also by their head-group properties – e.g., charge (nonionic, anionic, cationic or zwitterionic), size or chemical structure. Below we compare the results obtained with several types of surfactants, to clarify how these attributes affect the observed phenomena, see **Table 3**.

(a) Nonionic surfactants with 20 ethoxy groups in the hydrophilic head

First, we compare the results obtained with C₁₆EO₂₀ (see section 3.3), with those obtained with C₁₆SorbEO₂₀. These two nonionic surfactants have the same hydrophobic chain length and equal number of ethoxy groups in their hydrophilic heads, see **Table 3**. They differ, however, in the presence of a sorbitan ring in the head group of C₁₆SorbEO₂₀ and in the different structure of their ethoxy fragments – linear chain of 20 EO groups in C₁₆EO₂₀ vs. four separate fragments of approximately 5 EO groups in C₁₆SorbEO₂₀.

Figure 11A presents a comparison between the aspect ratios of hexadecane droplets, stabilized by C₁₆SorbEO₂₀ and C₁₆EO₂₀, as a function of temperature, at a cooling rate of 0.16 K/min and $d_{\text{ini}} \approx 31 \mu\text{m}$. One sees significant differences in the behavior of the two samples. Although the droplets stabilized by C₁₆SorbEO₂₀ start to evolve at a temperature close to the melting point of bulk hexadecane, $T_d \approx T_m$, and their shape evolves over a considerably wider temperature range of 6-8 degrees, the maximum aspect ratio which they reach is $AR = 5 \pm 1$ (platelets, see **Figures 4A** and **6B**). For comparison, much larger deformations, $AR = 90 \pm 10$, are observed with the other surfactant C₁₆EO₂₀, at a cooling rate of 0.16 K/min, because the platelets in the latter system emit thin long threads from their acute angles, as discussed in Section 3.2.

Figure 11B compares the deformations of the drops in the moment before their freezing, for surfactants C₁₆EO₂₀, C₁₆SorbEO₂₀ and C₁₈SorbEO₂₀. One sees that the surfactants, containing a sorbitan ring in their hydrophilic head, produce solid particles very similar in shape (hexagonal platelets) if the cooling rate is higher than 0.1 K/min and $d_{\text{ini}} \approx 30 \mu\text{m}$. To reach the next stages of the evolution scheme, we need to cool these emulsions at a very low cooling rate, $< 0.04 \text{ K/min}$.

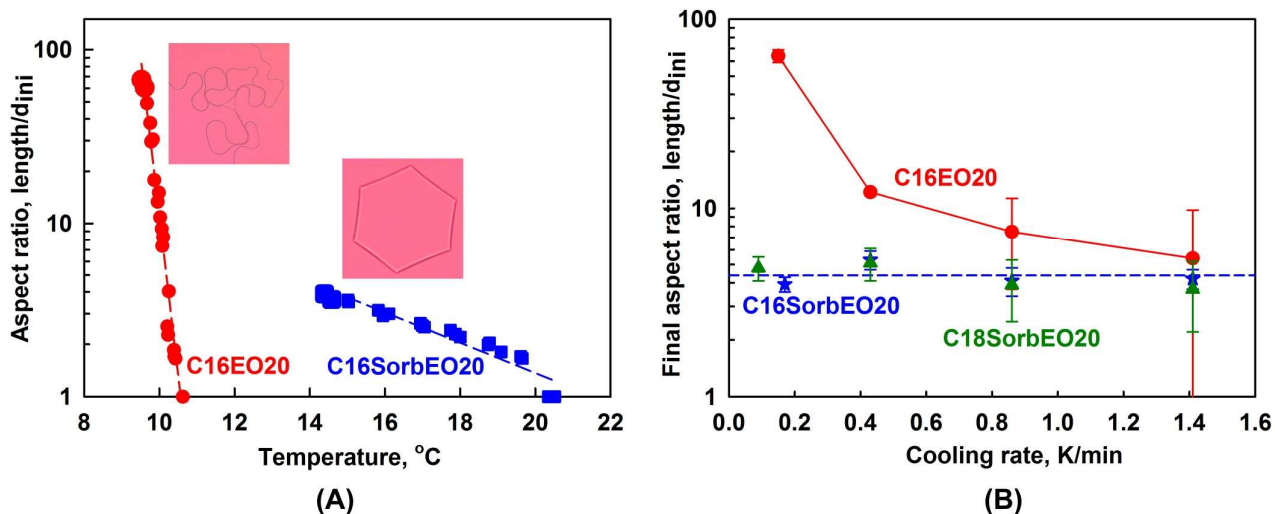


Figure 11. (A) Comparison of the individual droplet deformations, achieved from two monodisperse emulsions with drop diameter $d_{ini} \approx 31 \pm 3 \mu\text{m}$, stabilized by C₁₆SorbEO₂₀ and C₁₆EO₂₀, as a function of the sample temperature. Cooling rate is 0.16 K/min. (B) Final aspect ratio in the moment just before drop freezing, for droplets with diameter $d_{ini} \approx 31 \pm 3 \mu\text{m}$, which are cooled at different cooling rates and stabilized by various surfactants.

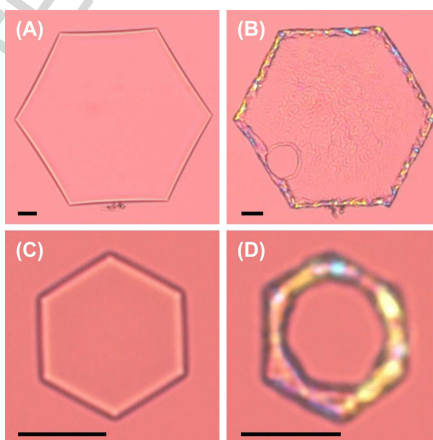


Figure 12. Images of (A, C) fluid and (B, D) frozen hexadecane droplets, stabilized by two different surfactants, both with well visible frames of cylindrical rods along the edges of the hexagons, stabilized by (A, B) C₁₆SorbEO₂₀ and (C, D) C₁₆EO₂. Scale bars, 20 μm .

Additional experiments with the other surfactants (see subsections (b) and (c) below) revealed that all studied surfactants could be classified into four distinct groups. In one of these groups we could combine C₁₆SorbEO₂₀ and C₁₈SorbEO₂₀ with C₁₆EO₂, while the other group comprises C₁₆EO₂₀ and CTAB (shown later as groups B and C in Table 4). Beside the other differences, these groups differ also with respect to the mechanical rigidity of the plastic crystal rods, forming a plastic frame at the periphery of the platelets or protruding from the drops as asperities and fibers. The rods formed in the presence of the first group of surfactants were very

rigid, thicker, and remained straight when encountering other rods upon their expansion or freezing, as illustrated in **Figures 12, 4D** and **Video 4**. Furthermore, for these surfactants, after the rigid rod frame at the drop periphery stretches the liquid interior so thin that it punctures in its central region, the droplets retain their outside shape and integrity, forming a toroidal in shape fluid drop, with a round hole in the middle, whose periphery in turn starts to deform (**Figure 13**). This would be possible only if the frame of the plastic crystal rods was strong enough to counteract the interfacial tension, trying to restore the spherical shape of the drops. In contrast, the rods stabilized by the second group ($C_{16}EO_{20}$ and CTAB) were softer and easily bent (cf. **Videos 1** and **2**).

Thus we see that the surfactant may affect strongly the initial temperature at which the drop deformations start, T_d , the range of typical drop shapes observed, and the thickness and rigidity of the rod-like and fiber-like structures formed.

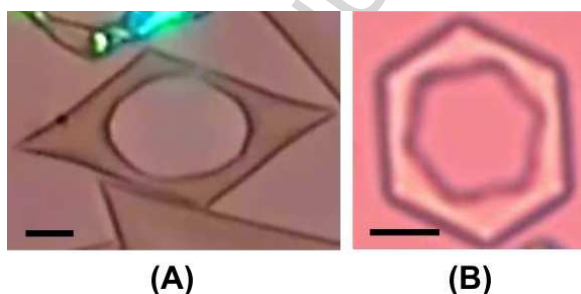


Figure 13. Images of flattened toroidal *fluid* drops, with a hole in their central region, stabilized by (A) $C_{16}SorbEO_{20}$ and (B) $C_{16}EO_2$. These holes confirm the liquid nature of the interior, the rigid outside frame of the shapes, and are different from the holes that form upon freezing of the shapes into crystals (e.g. Figure 12D). Scale bars, 10 μm .

(b) Role of the hydrophilic head-group size for C_nEO_m nonionic surfactants

In the experiments with the nonionic surfactants $C_{16}EO_{20}$ and $C_{16-18}EO_{25}$ we observed similar series of transformations, under equivalent conditions. In particular, the temperature at which the drops started deforming was similar, $T_d \approx 11^\circ C$, and the drops easily acquired high aspect ratios, although the entire process developed within 1-2 degrees of cooling before drop freezing, see **Figures 8** and **11A**.

On the other hand, experiments with other C_nEO_m surfactants, having smaller or larger head groups and/or longer alkyl chain-length, led to very different results. As mentioned already, the surfactant $C_{16}EO_2$, with a very small head-group, showed results resembling those with the sorbitan-containing surfactants – the drop shape transformations began at $T_d \approx T_m$ and continued along a temperature range of 6-8 degrees, up to platelets with $AR \approx 5$, see **Figure 13B**. These results clearly demonstrate that the reported differences between surfactant-stabilized C16 emulsions, exemplified in behavior by $C_{16}EO_{20}$ and $C_{16}SorbEO_{20}$ surfactants, are not related to the presence or absence of the sorbitan ring, but rather than to a different packing and different freezing point of the

surfactant at the surface (and probably related to that different packing and transition temperature for the oil phases template underneath), see Section 4.

Surfactants $C_{16}EO_{10}$, $C_{18}EO_{10}$ and $C_{18}EO_{20}$, characterized by longer tail or smaller EO head group (as compared to the reference $C_{16}EO_{20}$) showed rather different behavior from all the surfactants above (**Video 3**). First, the onset of drop deformation starts at a much higher temperature, in the range 20 to 23°C. After reaching the stage of a flat platelet in the evolutionary scheme, the oil layer in the center of the platelet is very thin and very often breaks. As a consequence, the deformed drop breaks abruptly, forming two or several new droplets with spherical shape. Note that the restoration of the spherical drop shape, after platelet puncture in its center, shows that the interfacial tension of these drops is not equal to zero, as it pulls back the drop into a shape with minimal surface area. The new droplets transform their shape again and after reaching the flat platelet stage, another breakage event is possible. Several consecutive cycles of these shape transformation/breakage events can be observed during a single cooling procedure, between one and ten times for most of the droplets. Thus, an efficient process of self-emulsification occurs without any mechanical energy applied to the emulsion.

Furthermore, for these surfactants ($C_{16}EO_{10}$, $C_{18}EO_{10}$ and $C_{18}EO_{20}$) flat platelets with different shapes and deformed drops, decorated with sharp conical edges like those shown in **Figure 7B**, readily formed and extruded long thin fibers (diameter < 1.5 μm). These thin fibers become very long, with aspect ratios well above 50. A capillary instability can be observed at this stage, leading to formation of many small ellipsoidal drops, connected to each other by thinner fibers with diameter $\leq 0.5 \mu\text{m}$ (the last stage in the evolution scheme). The tetragonal platelets may also undergo capillary instability or may release thin fibers until their final freezing.

Finally, surfactants of the C_nEO_m type, with excessively large surfactant head-groups, did not induce drop shape transformations. Examples are $C_{20-40}EO_{40}$ and $C_{16-18}EO_{50}$, containing 40 and 50 ethoxy groups, respectively. Whatever initial drop size and cooling rate were used with these surfactants, the alkane drops froze in a spherical shape, without any preceding shape changes. The C_{16} drops with $d_{\text{ini}} \approx 30 \mu\text{m}$ froze when supercooled down to $12 \pm 2^\circ\text{C} < T_m$, which indicates that surface nucleation still occurs (otherwise the drop freezing would occur at even lower temperatures, as for C_{12} surfactants, cf. section 3.3). Rather than templating a plastic crystal at the interface, however, the surface nucleation induced a direct alkane solidification in this case.

(c) Ionic surfactants

When using ionic surfactants with alkyl chain length similar or longer than that of the oil, we observed the same drop deformations as with the nonionic surfactants. For C_{16} drops with the anionic surfactant $C_{18}H_{37}SO_4Na$, the drop shape evolution was very similar to that described for the group of nonionic surfactants including $C_{18}EO_{20}$, $C_{16}EO_{10}$ and $C_{18}EO_{10}$, with respect to both the drop shapes observed and the temperature at which the transformations started ($T_d \approx 21^\circ\text{C} > T_m$). In contrast, the changes observed with the cationic surfactant CTAB were similar to those described

for the group containing C₁₆EO₂₀, although the drop deformation temperature was somewhat higher ($T_d \approx 14.5$ °C vs. 10-11 °C for C₁₆EO₂₀). Thus the ionic surfactants do not exhibit any distinct properties, as compared to the nonionic ones. One should be particularly careful, however, when working with cationic surfactants, because we often observed “sticking” and spreading of the hexadecane drops over the (originally negatively charged) glass surface – a process which could be easily mistaken with the internally driven evolution steps observed with the other surfactants.

Table 4. Groups of surfactants with respect to their effect on the drop “self-shaping” phenomenon for hexadecane (see text for explanations).

	Groups of surfactants	Main structural characteristic of molecules	Temperatures of drop deformation, T_d , and freezing, T_f	Preferred shapes	Interfacial layers' strength (thickness)
Group A	C ₁₆ EO ₁₀ C ₁₈ EO ₁₀ C ₁₈ EO ₂₀ C ₁₈ SO ₄ Na	Long tail and/or shorter EO chain Long tail anionic	$T_d > T_m$ $T_d \approx 19.5 \div 23^\circ\text{C}$ $T_f \approx 10 \div 15^\circ\text{C}$	Fibers with diameters ≈ 1.5 μm and ≤ 0.5 μm Different platelets and ellipsoidal drops extruding such fibers	Thin flexible layers
Group B	C ₁₆ SorbEO ₂₀ C ₁₈ SorbEO ₂₀ C ₁₆ EO ₂	Sorbitan ring Short EO chain	$T_d \approx T_m$ $T_d \approx 17 \div 19^\circ\text{C}$ $T_f \approx 12 \div 13^\circ\text{C}$	Hexagonal platelets Rods with diameter ≈ 5 μm The platelets do not extrude asperities from their corners	Very strong (thick) layers
Group C	C ₁₆ EO ₂₀ C ₁₆₋₁₈ EO ₂₅ CTAB	Larger EO head and/or shorter tail (C16) Long tail cationic	$T_d < T_m$ $T_d \approx 10 \div 11^\circ\text{C}$ $T_f \approx 8 \div 9^\circ\text{C}$ (nonionic) $T_d \approx 14.5^\circ\text{C}$ (CTAB) $T_f \approx 12.5^\circ\text{C}$ (CTAB)	All shapes are observed with a transition from rods with diameter ≈ 5 μm into fibers with diameter < 1 μm	Intermediate (soft rods)
Group D	Surfactants with C12-tail C ₂₀₋₄₀ EO ₄₀ C ₁₆ EO ₅₀ C _{18d} SorbEO ₂₀	Short tail Very large head-group Double bond in the tail	T_d not observed $T_f \approx 5$ to 8°C for short tails $T_f \approx 9$ to 13°C for large heads	Spherical	Not detected

From all these experiments we conclude that four categories of surfactants could be distinguished, based on their effect on drop shape transformations in C16 emulsions (see **Table 4**):

Group A: Surfactants inducing drop shape transformations above the bulk oil melting temperature, $T_d > T_m$. For hexadecane drops, the surfactants C₁₆EO₁₀, C₁₈EO₁₀, C₁₈EO₂₀, and C₁₈H₃₇SO₄Na fall into this group ($T_d \approx 21.5 \pm 2^\circ\text{C} > T_m \approx 18^\circ\text{C}$). The drops typically form thin flexible fibers with diameter ≈ 1.5 to $0.3 \mu\text{m}$, and various other shapes, such as platelets, with and without fibers protruding from their corners with acute angles.

Group B: Surfactants inducing drop shape transformations around the oil melting temperature, $T_d \approx T_m$. For hexadecane drops, the surfactants C₁₆SorbEO₂₀, C₁₈SorbEO₂₀, and C₁₆EO₂ fall into this group ($T_d \approx 18 \pm 1^\circ\text{C}$). They typically form hexagonal and other platelets (including fluid platelets which are punctured in their center) and relatively stiff rods with diameter $\approx 5 \pm 1 \mu\text{m}$, see **Figures 12** and **13**.

Group C: Surfactants inducing shape transformations at temperature T_d noticeably lower than T_m . For hexadecane drops, the surfactants C₁₆₋₁₈EO₂₅, C₁₆EO₂₀ and CTAB fall in this group ($T_d \approx 12 \pm 3^\circ\text{C} < T_m \approx 18^\circ\text{C}$). These surfactants easily create shapes in the entire evolution scheme (**Figure 3**), including various platelets, softer rods with diameter $\approx 5 \pm 1 \mu\text{m}$, and flexible fibers with diameter $< 1 \mu\text{m}$, see **Figure 8**.

Group D: Surfactants which do not induce drop shape transformations because their adsorption layers do not freeze before the freezing of the bulk alkane (e.g., surfactants with short chain-lengths or with tails containing double bonds) or the surface freezing leads directly to a liquid-solid phase transition, without formation of an intermediate rotator phase able to deform the drop surface (e.g., C₂₀₋₄₀EO₄₀ and C₁₆₋₁₈EO₅₀), see **Figure 6A**.

4. Discussion – mechanism of self-shaping

4.1. Main processes driving the observed drop shape transformations

The main processes which drive the observed drop-shape transformations were revealed in our recent study [43], see **Figure 14**. Briefly, the observed processes are triggered by a phase transition in the surfactant adsorption layer, at a temperature close to the alkane melting temperature, T_m . As explained in ref. [43], the bending moment of a single adsorption monolayer, even in a crystalline state, is insufficient to effectuate the observed drop-deformations. Indeed, the drop shape transformations start when the oil-water interfacial tension, γ , is of the order of several mN/m (typically, between 4 and 8 mN/m, see Section 4.4 below). Such an interface could be bent only under the following condition for the bending energy per unit area, $E_B \approx K_B/r^2 \geq \gamma$. Here K_B is the bending elasticity constant of the interface and $r \approx 1 \mu\text{m}$ is the characteristic curvature of the shaped droplet edges. Otherwise, for a lower bending energy, the requirement for a minimal

interfacial energy would pull the drop surface back to its initial spherical shape. Thus we estimate a minimum value for $K_B \geq 10^{-14}$ J, which is several orders of magnitude higher than the known bending constants of frozen lipid bilayers or surfactant adsorption monolayers, $K_B \approx 10^{-18}$ to 10^{-17} J [55,65-66]. Therefore, the drop deformation may be caused only by the presence of a multilayer of ordered self-assembled molecules which are able to create a sufficiently high bending moment to curve the drop surface against the drop surface energy and capillary pressure which both act as to preserve the spherical drop shape.

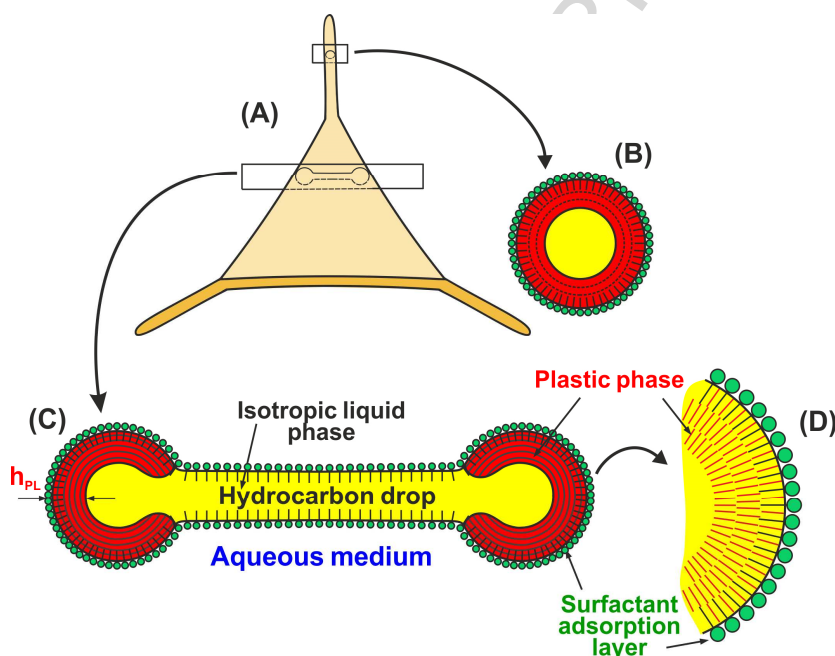


Figure 14. Schematic presentation of the mechanism of the observed phenomena. (A) Triangular platelet with protruding rods; (B) Cross-section of a rod with an external cylindrical shell of plastic rotator phase (red region) and inner liquid core (yellow region); (C) Cross-section of the platelet body with plastic rotator phase at the platelet periphery (red region) and liquid interior (yellow region); and (D) Interdigitated arrangement of the surfactant molecules (black tails) and alkane molecules (in red) in the surface layer, templating further ordered alkane layers (adapted from ref. [43]).

Though it is not able to bend the surface by itself, the “frozen” surfactant layer serves as a nucleation template for the formation of a multilayer of ordered alkane molecules (plastic rotator phase, see Section 4.2 below for further explanations), at locations with higher curvature on the surface of the alkane drops, **Figure 14**. Taking into account [66] that K_B is proportional to h_{PL}^2 , where h_{PL} is the thickness of the multilayer, generating the bending moment, we estimated that h_{PL} should be of the order of several hundred nanometres to generate a bending moment, sufficiently strong to curve the drop surface. Similar values of h_{PL} were reported in independent experimental studies for surface-induced liquid crystal sheet phases [67-68].

Furthermore, simple estimates show that the molecular energy gain of the plastic phase formation, $\Delta\mu_0$, is able to compensate the energy loss, related to the increase in the drop surface

area, ΔA , upon drop deformation, as explained below. For the purpose of estimates, we assume that the interfacial tensions of water-plastic phase and oil-plastic phase interfaces are equal and of the same “order of magnitude” as the water-liquid oil interfacial tension, $\gamma \approx 10$ mN/m. Then the energy penalty of drop deformation per unit area of the drop surface could be estimated per one molecule in the adsorption layer as $2\gamma A_0 \approx 4 \times 10^{-21}$ J ≈ 1 kT , where $A_0 \approx 0.2$ nm² is the area per molecule in the adsorption layer [69] and kT is the thermal energy (we include both the surfactant molecules and the interdigitated alkane molecules in the adsorption layer).

Since the formation of a plastic crystal in the drop is a phase transition, its energy change can be calculated as $\Delta E_{PL} = N_{PL}\Delta\mu_0 = (V_{PL}/V_M)\Delta\mu_0$, where N_{PL} is the number of hydrocarbon molecules included in the plastic phase which, in turn, can be found as a ratio of the volume of the plastic layer formed, V_{PL} , and the molecular volume of the hydrocarbon molecules, V_M . For supercooled drops, the change in the standard chemical potential of the hydrocarbon molecules upon the spontaneous phase transition from isotropic liquid into a plastic crystal phase, $\Delta\mu_0 = (\mu_{PL} - \mu_{OIL})$, is a negative value. Therefore, the energy gain in the process of formation of the plastic phase is the one that compensates for the expansion of the drop surface area and the related increase of the drop surface energy. One can estimate the energy gain per unit volume of the plastic phase as $\Delta\mu_0/V_M$ and by multiplying it by the layer thickness we get the energy gain per unit area of the deformed surface $h_{PL}\Delta\mu_0/V_M$. Noting that $V_M \approx lA_0$, where $l \approx 2$ nm is the length of the alkane molecule in the plastic phase and $h_{PL}/l \sim 10^2$ is the number of layers of alkane molecules in the surface plastic sheet (from the previous estimate above), one could estimate what value of $\Delta\mu_0$ is sufficient to compensate for the positive value of γ :

$$\Delta\mu_0 \geq -2\gamma A_0/h_{PL} \approx -4 \times 10^{-23} \text{ J} \approx -0.01 \text{ } kT$$

Note that $\Delta\mu_0$ has both enthalpic and entropic sub-components. The contribution of the entropic component is positive upon a phase transition which increases the molecular order, as it is the case for the liquid-to-rotator phase transition, studied in our experiments. Therefore, the entropic component opposes this phase transition. A negative enthalpic component, which is equal or bigger in magnitude than the entropic component, is needed to counterbalance the entropic component and to induce such a phase transition. Each of the enthalpic and entropic components is of the order of kT around the liquid-rotator phase transition, as measured by DSC [70]. The estimated small value of ≈ -0.01 kT is the difference between these two components, needed to compensate for the increased surface area of the deforming droplets. Thus we see that a tiny fraction of the thermal energy, kT , gained as a change of the Gibbs energy per molecule, is sufficient to overcome the increase in drop surface energy and to make stretching liquid droplets favorable.

New experimental results from the current study allow us to reveal further important elements in the underlying mechanism. Below we first introduce several relevant phenomena, related to rotator phases and surface nucleation (refs. [44,53,54,69-74]). Afterwards, we use these phenomena to explain the main experimental trends.

4.2. Surface nucleation and rotator phases

Surface nucleation is a widely studied phenomenon for alkanes and other hydrophobic molecules [73,74]. Numerous experiments with both flat interfaces [54] and drops [72] have shown that the surfactant chains freeze in the adsorption layer, in perpendicular orientation to the surface plane. Since the area per molecule of the surfactants (typically, between 0.3 and 1 nm²) [75] is much larger than the cross-section of the alkane molecules in the rotator phases, 0.20 ± 0.01 nm² [69], interdigitated alkane molecules in between the surfactant tails are certainly included in the frozen layers. From these areas per molecule one could estimate that the ratio of the interdigitated alkane molecules to surfactant molecules is between 1:2 and 4:1 for the various systems, see **Figures 14D** and **15**. The mixed layer of long surfactant tails and interdigitated alkane chains serves as a two-dimensional nucleus for growing of a neighboring bulk phase. Depending on the structure of the surface layer, it could serve as a template for different metastable or stable bulk phases.

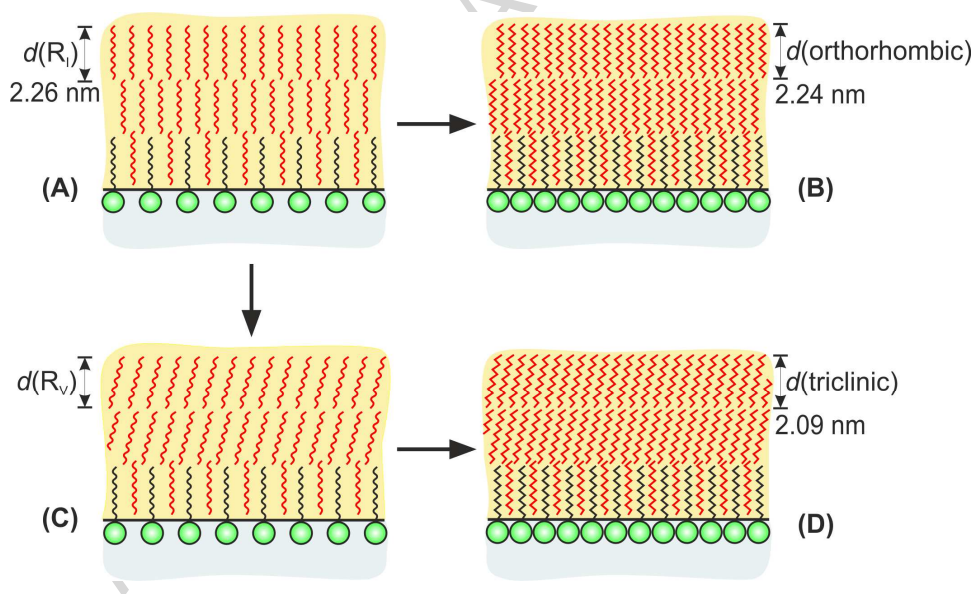


Figure 15. Schematic presentation of the molecular packing in (A) pseudo-hexagonal rotator phase R_I ; (B) orthorhombic solid phase; (C) rotator phase R_V ; and (D) triclinic solid phase. All phases are lamellar, with molecules directed perpendicularly (A, B) or tilted (C, D) to the lamellar planes. The molecules in the non-frozen phases (A, C) have some rotational freedom along the longest molecular axis. All these phases were reported for the alkanes in the range studied here, except for the rotator phase R_V which was reported for longer alkanes only (C22-C28), so far.

The rotator phases appear as intermediate phases when long- and intermediate-chain alkanes are cooled, along their transition from isotropic liquid phase to a completely frozen solid phase [44]. Several rotator phases were described which differ in their stability (stable, metastable or transient) and the positional arrangement of the alkane molecules [44,71]. Most of these phases were observed

with alkanes of longer chains (C22 to C45) than those studied here (C14 to C20). In the following discussion we focus mainly on the rotator phase which was observed with alkanes within the range of chain-lengths studied here. This phase is usually called in the literature “pseudo-hexagonal” rotator phase and is denoted as R_I [70]. This phase is a lamellar structure, with the alkane molecules stacked perpendicularly to the lamellar planes and being able to rotate or vibrate around their long axis, see **Figure 15A**. For hexadecane the period of lamella spacing is 2.26 nm in the R_I phase [72]. Upon cooling, the alkane molecules could freeze without changing their tilt with respect to the lamella plane, into the so-called “orthorhombic” solid phase, **Figure 15B**.

When bulk alkanes in the range C14 to C20 were studied, the R_I phase was observed as stable or metastable, only with alkanes having an odd number of carbon atoms (e.g., C17 and C19) [71]. The bulk hexadecane and the other alkanes with even number of carbon atoms in this range (C14 to C20) usually pass from an isotropic liquid phase, via transient (very short-lived) rotator phase, into a solid triclinic phase with tilted molecules with respect to the lamellar planes (**Figure 15D**). This tilt leads to a smaller lamella period, e.g. 2.09 nm for the triclinic hexadecane crystal [72]. Note that structurally more similar to the triclinic phase is another rotator phase with tilted molecules, denoted as R_V in the literature [44], **Figure 15C**. Phase R_V was observed with a wide range of alkanes with longer chains (C22 to C28). It appears as the last intermediate phase between the other rotator phases occurring at higher temperature (R_I to R_{IV}) and the final solid phase [44].

On the other hand, if surfactants with long surfactant tails, such as C_{16} and C_{18} , are used to stabilize micrometer-sized emulsion drops, R_I phase appears spontaneously in emulsion drops of the alkanes with even number of C-atoms (C16, C18 and C20), as shown by SAXS, WAXS and DSC data by Ueno et al. [72]. The appearance of rotator phases in drops of these alkanes could be explained only by assuming that the curved drop surfaces favor thermodynamically the molecular self-assembly into plastic rotator phases for these alkanes. Furthermore, solidification of the formed R_I phase into an orthorhombic solid phase, **Figure 15B** (instead of the triclinic solid phase, **Figure 15D**) was reported in such drops. The explanation given [72] is that the frozen adsorption layer with perpendicularly oriented molecules (with respect to the drop surface) serves as a template for the growth of the R_I rotator phase and subsequent freezing into the structurally similar orthorhombic solid phase in the hexadecane droplets.

As explained in Section 4.3 below, we have substantial experimental evidence that two rotator phases may appear before the oil freezes in the observed shape-changing drops. Therefore, R_I as a higher temperature rotator phase, and R_V as a lower temperature rotator phase (or their structural analogues, as explained in Section 4.3B below) are the most probable phases encountered in our experiments.

4.3 Explanations of the main observed trends.

(A) Onset of drop deformation and general evolution scheme

The fact that we need long-chain surfactants to trigger the observed phenomena proves that the process certainly starts with a phase transition in the surfactant adsorption layer. The drop deformation starts with formation of convex pikes on the drop surface which, within seconds, transform into the tips of a regular polyhedron. These pikes are of micrometer size and are too large to be the actual surface nuclei. Therefore, these pikes contain an already confined rotator phase. Note that the deformation of the drop surface involves a penalty for the increased surface area and the related increase of surface energy. As demonstrated in **Section 4.1**, the self-assembly of the molecules in the rotator phase leads to energy gains which easily overcome the energy loss, created by the surface stretching – a very small fraction of the thermal energy kT per self-assembled alkane molecule is sufficient to ensure a sufficient energy gain.

Our observations show that, once the process is initiated, the alkane molecules spontaneously self-assemble into cylindrical rods of a plastic rotator phase, **Figure 14**. In this way, a frame of gradually elongating, interconnected cylindrical rods is formed at the drop surface, which expands with time via incorporating more and more molecules from the liquid interior of the drops. This process gradually stretches the drop surface and creates a series of symmetry breaking events in the frame. This evolution through multiple shapes indicates that the additional energy of extending the plastic phase cylinder is comparable to the interfacial energy which modulates it. The balance of these energies (and the related forces) brings about the complex shape evolution, sketched in **Figure 3**.

We are still unable to predict theoretically the full sequence of events – the respective theoretical modeling is a challenging task which is beyond the scope of the current study. We note, however, that the observed shapes satisfy the principle of “tensegrity” – a branch of science and engineering, named as a portmanteau of the term “tensional integrity” [76]. In accordance with the laws of tensegrity, the compression created by the interfacial tension of the stretched drop surface is counter-balanced by the mechanical strength of the self-assembled frame of plastic crystal rods. As a result, most of the observed shapes are Platonic polyhedrons or flat platelets (hexagons, triangles) in which the respective stresses are balanced.

One very particular feature of our system is that the “tensegrity” rods can spontaneously grow or shrink via exchange of molecules with the adjacent liquid phase and with the other plastic rods. The fact that the rods meeting at the platelet corners are able to balance the force of the interfacial tension, and may reversibly shrink or grow around the equilibrium shape (e.g. of hexagonal or triangle platelets) is evidence that the force exerted by the growing plastic crystal edges is of the same order of magnitude as the force generated by the oil-water interfacial tension in the presence of surfactant. The effect of interfacial tension can be expressed via the capillary pressure of the deformed interface, $P_c \approx \gamma/r \approx 10^4$ Pa, where $r \approx 1 \mu\text{m}$ is the characteristic radius of curvature of the platelet edges and of the rods and fibers. Therefore, the frame is able to “push” the surface with a

pressure of the same order (or higher) and with the respective force, $F_f \geq P_c r^2 \approx 10^{-8}$ N, where F_f is the force of the condensing rotator phase against the droplet surface, in direction perpendicular to the rod axis.

The energy of the alkane molecules, self-assembled in the cylindrical domains is lower than that of the molecules in the isotropic liquid phase, see **Section 4.1** and **Figure 16A**. The latter statement is supported by the numerous experimental observations that the flat region in the center of the evolving platelets thins down to thicknesses which are much smaller than the diameter of the plastic rods forming the frame – see for example the image in **Figure 12** where the cylindrical rods have a diameter of 5 μm , whereas the thickness of the central region was estimated from drop volume conservation to be only ≈ 0.4 μm . In other words, the curved cylindrical plastic regions at the drop periphery “suck out” molecules from the central planar region which remains in a liquid state during this process. Similarly, the rod-like asperities and fibers growing from the platelet edges, suck-out molecules from the liquid drop interior, as seen in **Video 1** and **Video 2**.

(B) Two stages in the evolution scheme – two rotator phases involved

One generic feature of the evolution scheme, expressed through the changes in the drop aspect ratio $AR(t)$ or $AR(T)$ (see **Figures 9** and **10**), could be used to analyze further the role of the rotator phases in the observed phenomena. The graphs about the evolution of the drop aspect ratio vs. time (**Figures 9-10**) show two distinct regions of drop shape evolution for small and large aspect ratios, respectively. In the first region the transformations are relatively slow and we could stop, and drive forward and backward the drop shape using fine control of temperature. This region includes the stages of the polyhedra and the platelets, including the systems in which cylindrical rods with diameter of several micrometers are extruded from their sharp tips (**Figure 3, Stage 1**).

The second region starts with the stage in which sub-micrometer fibers are formed, and it is qualitatively different. These fibers might appear either as a result of capillary instability of the thicker cylindrical rods (**Video 1**), or could be extruded from platelet corner tips with sharp angles directly or from the conical tips on the surface of ellipsoidal drops (in both last cases the angle at the fiber extruding tip is around $30 \pm 15^\circ$, **Video 2**). As seen from **Figures 9** and **10**, the aspect ratio in the second region increases by an order of magnitude faster as compared to the first region. More importantly, we could not control the observed process of capillary instability – the thick rods expanded and evolved into thin fibers at all cooling rates we tried. Furthermore, upon heating we observe a different pathway in the shape transitions – the thin fibers do not reverse back to the thicker cylindrical rods from which they have appeared. Upon slow heating, the thin fibers do retract and are directly sucked back into the liquid drops, but they skip the intermediate geometric shape changes. These observations provide evidence that the transition between the thicker rods and thin fibers is not reversible in the time-scale of our experiments.

Based on the above observations, we assume that these two distinct regions in the evolution scheme correspond to the presence of two rotator phases. The rotator phase formed at higher temperature is expected to be similar to R_1 , because this is the only rotatory phase reported for the

alkanes studied (in bulk or in drops). For the low temperature phase, we speculate that it is probably a cylindrical analog of phase R_V , described above, because its tilted layer structure is intermediate between R_I and the solid triclinic phase, typical for the frozen C16 and C18 alkanes.

We should note that the preferred cylindrical confinement of the self-assembled molecules requires rotator phases with structures which are not exactly identical to the R_I and R_V phases (which are planar by definition), **Figure 16A**. The cylindrical arrangement corresponds to less molecules in the inner layers, at the same area per molecule in the respective layers, see **Figure 14D**. For example, if we have hexadecane multilayers with period of 2.26 nm, for a radius of layer curvature $\approx 1 \mu\text{m}$ each next inner layer should have 0.226 % fewer molecules. To account for this required difference in the structures of the rotator phases observed in the bulk alkanes and in the small alkane droplets, we denote the latter phases as R_{CI} and R_{CV} , where the subscript “C” denotes “cylindrical”.

Concluding, based on the experimental observations we assume that R_{CI} phase is formed first at higher temperature [44], followed by the transition $R_{CI} \rightarrow R_{CV}$, when the thin fibers appear. The energy landscape of the various phases and the related phase transitions [71] are illustrated in **Figure 16B**. The R_{CV} phase has properties intermediate between the R_{CI} phase and the solid, so we postulate its free energy slope is between those two phases. The approximate intersections in **Figure 16B** are drawn in a way allowing us to reproduce the observed phase transitions, which start at different temperatures with the various surfactant types, as explained below.

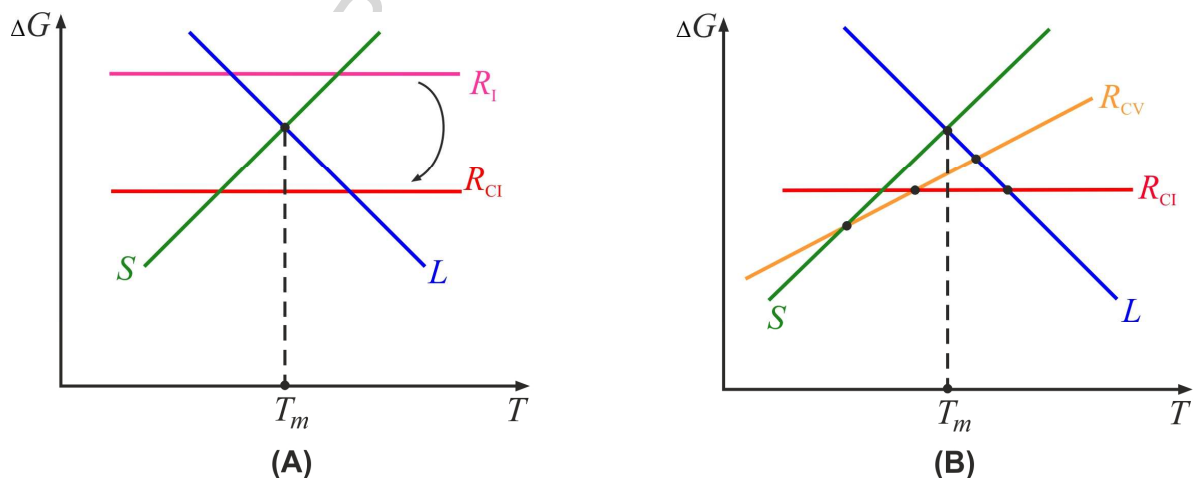


Figure 16. Energy diagrams for the liquid (L), solid (S) and rotator phases (R) involved in the observed phase transitions, with ΔG denoting the energy difference with respect to the rotator phase R_{CI} . (A) The energy of the rotator phase decreases when it is formed next to a curved interface which makes the cylindrically packed version of the rotator phase R_{CI} more stable than the solid or liquid for temperatures near T_m . (B) From the experimental results one can deduce that two rotator phases are involved in the drop shape transitions, denoted as R_{CI} and R_{CV} . The intersections are approximate and are drawn in a way to allow reproducing the observed phase transitions, which start at different temperatures with the various surfactant types, cf. with Table 4 and Figure 17.

(C) Effect of the surfactant type

The data in **Table 4** indicate that the surface nucleation, which triggers the drop deformation phenomenon, depends strongly on the type of surfactant used. As already mentioned, all surfactants studied could be grouped into four groups:

Surfactants containing sorbitan ring (e.g., C₁₆SorbEO₂₀) and those with small head groups and/or longer tails (C₁₆EO₂, C₁₆EO₁₀, C₁₈EO₁₀ and C₁₈EO₂₀) induce drop shape transformations at a temperature above and around the alkane melting temperature, T_m . Hence, these surfactants create easily a surface nucleus with appropriate structure to induce the formation of the R_{CI} rotator phase around the curved interface. Upon further cooling, R_{CI} phase transforms into the other rotator phase (presumably R_{CV}) and the drops finally freeze. These are the surfactant in **groups A and B** and their phase transitions are illustrated on the energy diagrams in **Figures 17A and 17B**, respectively.

Surfactants C₁₆EO₂₀, C₁₆EO₂₅ and CTAB (**group C**) behave differently, as they induce drop shape transformations at temperatures which are well below the alkane melting temperature, $T_d < T_m$. Therefore, these surfactants do not create a surface nucleus with appropriate structure to induce the R_{CI} phase around T_m . It is still an open question whether they form such nucleus at a lower temperature or, alternatively, they create a nucleus for directly growing the R_{CV} phase. From the fact that these surfactants first lead to the formation of micrometer in diameter asperities, which afterwards undergo a transition into thin fibers, we assume that the R_{CI} phase is induced first, although at a lower temperature (**Figure 17C**).

Surfactants with short chain length (C₁₂), those with excessively large head groups (EO₄₀ and EO₅₀), and those with a double bond in the middle of their alkyl tail (C_{18d}) do not induce drop shape transformations and the drops freeze directly into solid alkane spheroids, typically at significant supercooling. Obviously, these surfactants are unable to nucleate rotator phases in the appropriate temperature range and a hexadecane solid phase is directly formed, as a result of either bulk or surface nucleation (**group D; Figure 17D**).

Note that the supercooling effect, which leads to an evolution not via the lowest energy phase path (**Figure 17C-D**), is a well pronounced phenomenon for emulsions, due to the low probability for nucleation in the small emulsion droplets [62-64]. As a result, metastable phases with higher energy might be easily formed in the emulsion droplets, if the barrier for their formation is lower than the barrier leading to the phase with lowest energy. This situation is illustrated in **Figure 18** for a rotator phase (with higher energy and lower barrier) which might appear first as a metastable intermediate phase, instead of the stable solid phase (with lower energy and higher barrier).

Note also that the structure of the solid phase in the completely frozen drops could be different, depending on the surfactant templating, cooling conditions and drop size. If the solid phase is nucleated in the liquid drop interior (bulk nucleation) or from a R_{CV} rotator phase with tilted molecules, a triclinic solid phase is expected to appear. If the solid phase is nucleated from the R_{CI} phase with perpendicular molecules, then the orthorhombic solid phase could appear. Indeed,

Shinohara et al. [77] reported the formation of both solid phases, triclinic and orthorhombic, in their experiments.

It is worth emphasizing that the cooling rate of 2 °C/min, used in the experiments which demonstrated the existence of the R_I phase in hexadecane emulsion droplets [72], was relatively high, when compared to the rates needed to proceed through the complete evolution scheme in **Figure 3**. Therefore, if any shape changes occurred (not reported) during the experiments in ref. [72], they would have been only part of the first stage of this scheme. Additional phenomena (e.g., the occurrence of R_{CV} or other rotator phases) could be observed if the same experimental methods were applied at a lower cooling rate and with different surfactants.

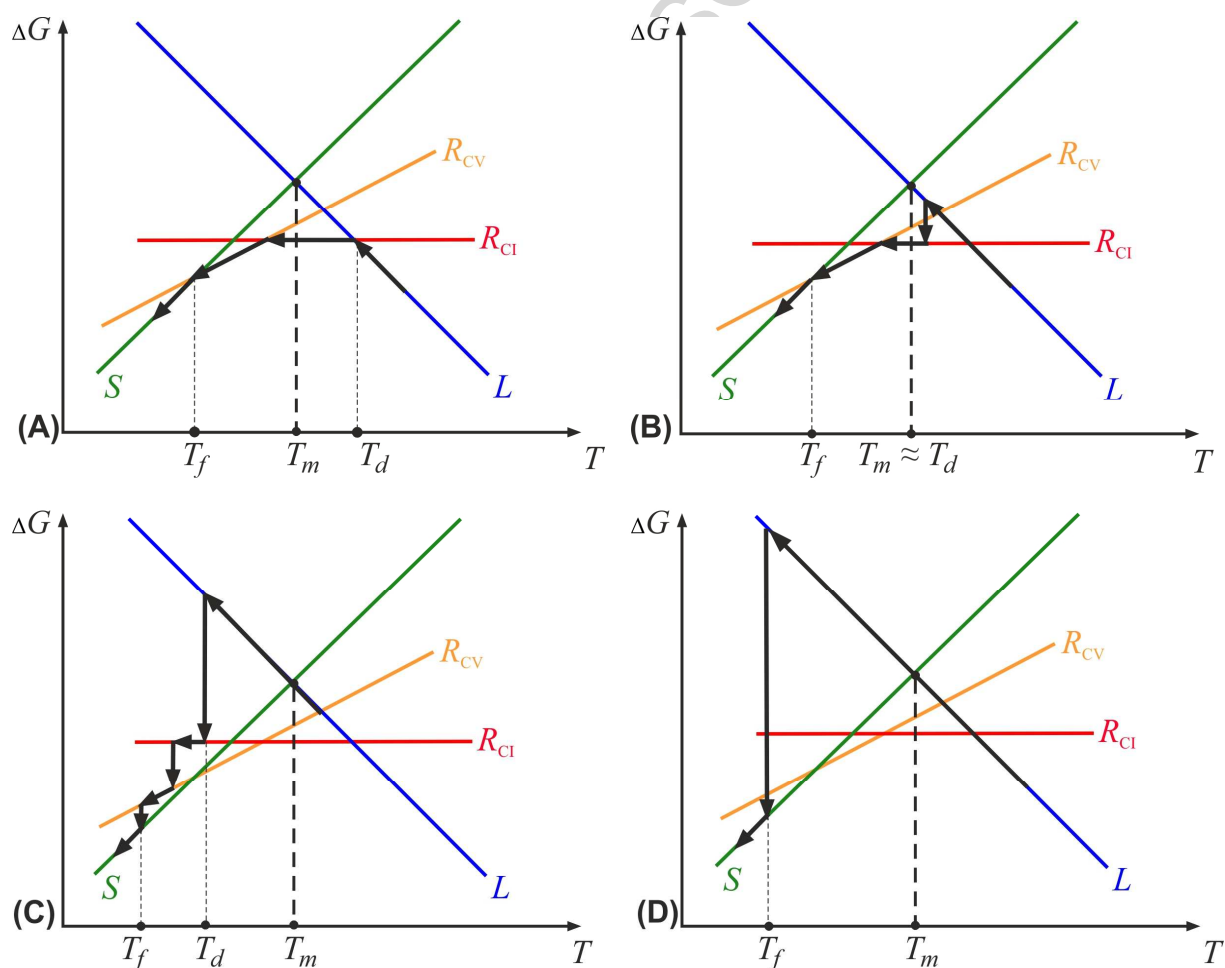


Figure 17. Arrows showing the phase paths upon emulsion cooling, in the presence of stable intermediate rotator phases R_{CI} and R_{CV} , drop deformation starting at temperature T_d , and drop freezing at temperature T_f . (A) Minimum energy path $L \rightarrow R_{CI} \rightarrow R_{CV} \rightarrow S$, corresponding to drop deformation starting at $T_d > T_m$ and corresponding to surfactants from **group A** in **Table 4**. (B) Evolution path for drop deformation starting at $T_d \approx T_m$ (**group B**). (C) Evolution path for drop deformation starting at $T_d < T_m$ (**group C**). In (B) and (C) supercooling in the transition $L \rightarrow R_{CI}$ occurs, while the overall sequence of transitions is the same as in (A). (D) direct solidification $L \rightarrow S$ after large supercooling (**group D**).

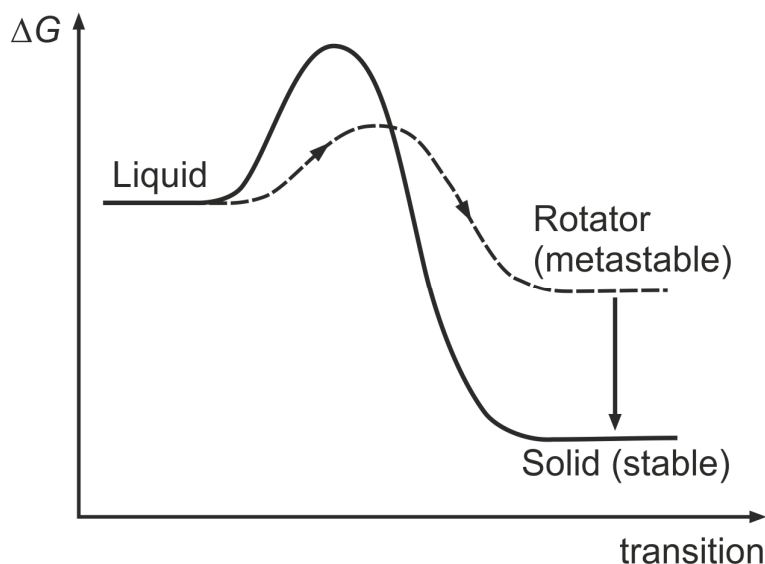


Figure 18. Energy diagram, illustrating the possibility for formation of a metastable phase, when the barrier to nucleate it is lower, compared to the barrier to nucleate and reach the globally stable state for a given temperature. The case of stable solid and metastable rotator phase is shown here, but similar diagrams may apply for the transitions involving two rotator phases. The barriers are lower for transitions between phases which are structurally similar (e.g. R_I to orthorhombic solid phase or R_V to triclinic solid phase).

(D) Effects of the drop size and cooling rate

The results from all our experiments showed that, for a given surfactant and a given alkane, bigger deformations are achieved with smaller droplets and at lower cooling rates. Indeed, the cooling of a mixed size population of drops led to deformation onset at approximately the same temperature, however, the smaller droplets evolved much faster and further along the evolution path before they froze.

The effect of drop size is related to the effect of curvature on the energy of the plastic rotator phase. As already explained, stable and metastable rotator phases with C16, C18 and C20 alkanes were reported only in emulsion droplets, whereas only transient, very short-lived rotator phases were reported for bulk alkanes of this molecular size [71]. This means that the drop surface curvature is essential to reduce the energy of transformation to these rotator phases, as shown in **Figure 16A**. One could expect that the optimal curvature for rotator phase formation is close to that of the spontaneously forming rod-like and fiber-like asperities, i.e. around 3 to 5 μm in diameter for the R_{CI} phase and below 1 μm for the lower-temperature rotator phase (presumably R_{CV}).

Concerning the effect of the cooling rate, see **Figure 9**, it clearly shows that the rates used (although being the slowest ever reported in such studies) are still too fast to allow the establishment of a true equilibrium, especially at high aspect ratios when long cylinders and fibers

are extruded from the drops. The main reasons are the peculiar rheological properties of the plastic rotator phases and the high aspect ratio of the droplets – the relaxation times for such systems could be very long and the equilibrium might be difficult or impossible to achieve in the experimentally accessible time scale. Therefore, we expect that the drops would follow the entire path in the evolution scheme, if cooled sufficiently slowly. In the real experiments, however, the drops are supercooled without being able to relax to the respective equilibrium shape – as a result, the drops end up being trapped and then frozen in a shape mid-way along the transformation scheme.

4.4. Critical comparison of our experimental results with the explanation assuming ultra-low interfacial tension

At the end of the discussion section, let us mention a recent study [55], published soon after our previous paper [43], and reporting similar observations with the system C16/C₁₈TAB, which we did not specifically study. This system is very similar to ours and, not surprisingly, many of the experimental observations resemble those reported in ref. [43] and in the current study. However, the major points in the mechanistic explanation of the observed phenomenon, proposed in ref. [55], differ qualitatively from our explanations. In particular:

- (1) Ultralow interfacial tension ($\gamma \ll 1$ mN/m) was reported by Guttman et al. [55] at temperatures below the freezing temperature of the surfactant adsorption layer. Even temporary negative tension was proposed to explain the formation of rod-like asperities.
- (2) Guttman et al. [55] did not consider the possibility for formation of rotator phases in the hexadecane drops. Instead, the measured ultralow interfacial tension was used to explain that there should be a very small or non-existent energy penalty for increasing the surface area of the droplets.
- (3) The observed drop deformations were explained with the assumed tendency of the frozen surfactant monolayer to acquire a flat shape. “Tiling” of the spherical drops with flattened facets of frozen surfactant layer was assumed to explain the formation of icosahedral droplets at the onset of drop deformation.

Because the experiments in ref. [43] are performed with different substances, we would not perform an exhaustive analysis of the differences between the various systems we studied and the system studied in ref. [55]. Instead, we demonstrate below that the explanations, proposed by Guttman et al. [55] for their system, could not explain the phenomena observed in our experiments:

Interfacial tension. We measured the interfacial tension of a large number of systems, using a drop shape analysis of pendant drops, immersed in surfactant solutions, in the temperature range in which the drop deformations were observed. We have never observed ultra-low interfacial tension (lower than ca. 1 mN/m) like that reported in ref. [55] – see **Figure 19** with illustrative data for two of the samples studied. Furthermore, our measurements of the interfacial tension of such drops did not show any specific kink in the curves $\gamma(T)$ around the onset temperature of drop deformation, T_d

– see **Figure 19**. This lack of correlation between $\gamma(T)$ and T_d indicates that the drop deformation may start with the formation of a local surface nucleus, without a complete pre-freezing of the adsorption layer that would be detected by the pendant drop method. Furthermore, the formation of such surface nuclei and/or their further development into a bulk rotator phase should be easier for the smaller droplets with higher surface curvature, as evidenced by the fact that the large millimeter-sized pendant drops do not deform at the temperatures, at which the micrometer droplets have evolved deep into the self-shaping phenomenon.

The fact that the platelets transform immediately back to spherical drops upon droplet breakup in most experiments (see **Video 3**), is another direct proof that the platelets do not have ultralow interfacial tension. Note that the drop breakup in **Video 3** occurs most probably via puncturing in the platelet central region (where the thinnest part of the platelets is formed) which is not seen in this movie, but is well seen in other systems – see e.g. **Figures 12** and **13**. Furthermore, the initial circular shape of the holes formed in this process (see **Figure 13A** for example), is another proof that the interfacial tension is not ultra-low in these systems. The hexagonal shape of the holes, like those shown in **Figure 13B** develops afterwards, as rods of plastic phase form in the region of high interfacial curvature at the hole periphery.

Therefore, we could not explain the observed changes with the ultralow interfacial tension, with the “tiling hypothesis”, and with the bending moment of the surfactant monolayer (it is far too weak), as proposed in ref. [55].

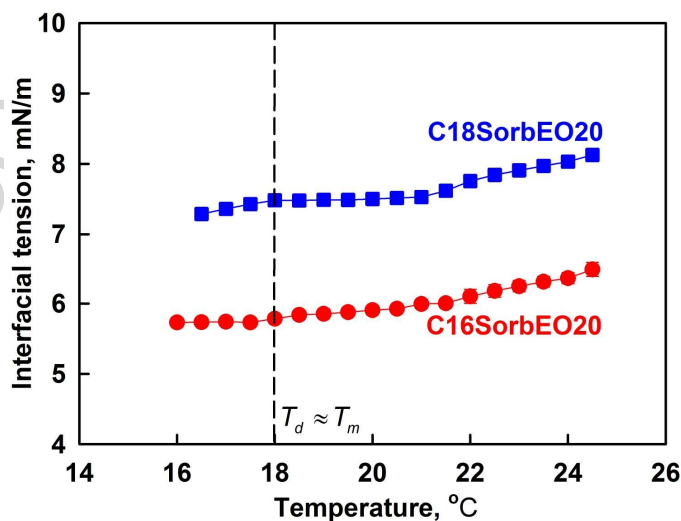


Figure 19. Interfacial tension as measured by the pendant drop method, as a function of temperature, for hexadecane drops immersed in the aqueous solutions of two different surfactants, as indicated in the figure. The experimental error in determining the interfacial tension is ± 0.1 mN/m. The vertical dashed line denotes the melting point for hexadecane (T_m), which coincides with the initial droplet deformation temperature for these surfactants ($T_d = T_m \pm 1$ °C, explained also in Table 4).

Formation of cylindrical asperities. The formation of cylindrical borders of the platelets and of the rod-like asperities shows clearly that our systems exhibit a spontaneous curvature with radius in the micrometer range. The assumption for the formation of flat interfaces, proposed by Guttman et al. [55], could not explain the formation of the observed cylindrical objects.

Many of the observed bodies appear as rather stiff – see for example our **Video 4** which shows the collisions of expanding cylindrical rods. We have not been able to measure directly the stiffness of these objects yet, but the lack of deformations upon their collisions shows that these rods do not have ultralow interfacial tension and a weak bending moment – otherwise they would be much more flexible.

Based on the above arguments we conclude that our experimental results could not be explained by the assumptions made in ref. [55].

5. Conclusions.

More than 60 different combinations of organic liquids and surfactants were investigated (see **Tables 1, 3 and S1**) to clarify the mechanism of the drop “self-shaping” phenomenon, described in ref. [43]. The main conclusions from this study could be summarized as follows:

We show for the first time that this phenomenon is possible not only with linear alkanes but also with a wide range of other organic molecules, representing the classes of long-chain alcohols, triglycerides, alkyl cyclohexanes, and linear 1-alkenes. This newly demonstrated variety of chemical systems, exhibiting this phenomenon, hints to the possibility that it might be much more general than initially thought [43] – the drop “self-shaping” spectacle might be typical for various classes of chemicals which contain a sufficiently long linear chain in their molecules and appropriate packing dimensions.

All systematically studied alkane systems followed the general evolution scheme shown in **Figure 3**. The main differences were in the onset temperature of drop deformation, drop freezing temperature, and the final drop deformation in the moment of solidification. The drop-shape evolution is more pronounced for smaller drops, lower cooling rates, and for longer surfactant alkyl tails compared to the oil alkane chain. These general trends are explained by considering the properties of the rotator phases, formed in alkane drops.

Surfactants affect the overall process in three main aspects: (a) the temperature at which the shape transformations start; (b) the final aspect ratio of the frozen particles; and (c) the appearance of rods or fibers with micrometer or sub-micrometer diameter, respectively. Depending on the surfactant and cooling rate, one or another branch in the evolution could occur with higher probability. On this basis, one can classify all the surfactants studied into four groups, as shown in **Table 4** and explained in sections 3.4 and 4.3.

The obtained results are important for several research areas. First, we have demonstrated that a remarkably simple chemical system (alkane drop, decorated with an appropriate long-chain surfactant) may show complex structure and shape transformations, similar to those observed in living organisms. Second, the use of appropriate surfactants and cooling rates could be the key for driving the observed processes into a desired direction. Third, the subtle interplay between the molecular self-assembly into cylindrical plastic phases, and the effects of frustrated confinement, interfacial tension and surface curvature result in complex elasto-capillary transitions, governed by the laws of tensegrity, and provide a unique tool-box for studying these and other related phenomena. Fourth, the method could be applied to synthesize a large variety of particles with complex shapes, especially when combined with other methods for particle synthesis. The fact that this self-shaping phenomenon occurs with functional molecules, such as alkenes and alcohols, allows one to use chemical reactions for polymerization of the deformed droplets and/or surface modification of the obtained solid particles.

Acknowledgements:

This work was funded by the European Research Council (ERC) grant to Stoyan Smoukov, EMATTER (# 280078). The study falls under the umbrella of European networks COST MP 1106 and 1305. The authors are especially grateful to Prof. Howard Stone (Princeton Univ.) for the illuminating discussions and suggestions, Prof. Richard Gordon for suggesting looking at the droplets as tensegrity structures, Ms. Mila Temelska for measuring interfacial tensions, and Dr. Konstantin Golemanov for the useful discussions.

References

1. Turing A, *Phil. Trans. R. Soc. London*, 1952; 237:37-72.
2. Newman SA, Forgacs G, Muller GB, *Int. J. Dev. Biol.*, 2006; 50:289-299.
3. Newman S, Comper W, *Development*, 1990; 110:1-18.
4. Savin T, Kurpios N, Shyer A, Florescu P, Liang H, Mahadevan L, Tabin CJ, *Nature*, 2011; 476:57-62.
5. Kim J-W, Larsen R, Weitz D, *J. Am. Chem. Soc.*, 2006; 128:14374-14377.
6. Ding T, Baumberg J, Smoukov SK, *J. Mater. Chem. C*, 2014; 2:8745-8749.
7. Wulff G, *Z. Krystallogr. Miner.*, 1901; 34:449-530.
8. Stranski IN, *Zur Theorie der Kristallwachstums. Z. Phys. Chem.*, 1928; 136:259-278.
9. Volmer, M, "Kinetic der Phasenbildung", T. Steinkopf, Dresden, 1939.
10. Burton, WK; Cabrera, N; Frank, FC, *Philos. Trans. Royal Soc. A*, 1951; 243:299-358.
11. Alberts B, Johnson A, Lewis J, Morgan D, Raff M, Roberts K, Walter W, *Molecular Biology of the Cell*, Garland Science 2014.
12. Pross A, *What Is Life?: How Chemistry Becomes Biology*, Oxford University Press, 2012.
13. Venkataram Prasad BV, Schmid MF, *Adv. Exp. Med. Biol.* 2012; 726:17-47.
14. Klug A, Caspar DL, *Adv. Virus Res.* 1960; 7:225-325.
15. Johnson JE, Speir JA, *J Mol Biol.* 1997; 269:665-675.
16. Rey C, Combes C, Drouet C, Glimcher MJ, *Osteoporos Int.* 2009; 20:1013-1021.
17. Simmer JP, Fincham AG, *Crit Rev Oral Biol Med.* 1995; 6:84-108.
18. Sun J, Bhushan B, *RSC Adv.* 2012; 2:7617-7632.
19. Simkiss K, Wilbur KM, *Biom mineralization*, Elsevier 1989.
20. Hotze EM, Phenrat T, Lowry GV, *J. Environ. Qual.*, 2010; 39:1909-1924.
21. Walther A, Müller AHE, *Soft Matter*, 2008; 4: 663-668
22. Baule A, Makse H, *Soft Matter*, 2014; 10:4423-4429.
23. Wolf B, Frith W, Singleton S, Tassieri M, Norton I, *Rheologica Acta*, 2001; 40:238-247.
24. Xiao J, Qi L, *Nanoscale*, 2011; 3:1383-1396.
25. Peng, X. et al. *Nature*, 2003; 2:145-150.
26. Kuo C, Huang M, *J. Phys. Chem. C*, 2008; 112:18355-18360.
27. Lisiecki I, Billoudet F, Pileni M, *J. Phys. Chem.*, 1996; 100:4160-4166.
28. Lisiecki I, *J. Phys. Chem. B*, 2005; 109:12231-12244.
29. Alargova R, Bhatt K, Paunov V, Velev O, *Adv. Mater.*, 2004; 16:1653-1657.
30. Dendukuri D, Doyle P, *Adv. Mater.*, 2009; 21:4071-4086.
31. Smoukov SK et al., *Adv. Mater.*, 2015; 27:2642-2647.
32. Almería B, Deng W, Fahmy T, Gomez A, *J. Colloid Interface Sci.*, 2010; 343:125-133.
33. Noble P, Cayre O, Alargova R, Velev O, Paunov V, *J. Am. Chem. Soc.*, 2004; 126:8092-8093.

34. Dinsmore A, et al., *Science*, 2002; 298:1006-1009.
35. Jonas U, Vamvakaki M, *Angew. Chem. Intern. Ed.*, 2010; 49:4542-4543.
36. Sukhorukov et al., *Colloid Surf. A*, 1998; 137:253-266.
37. Rudhardt D, Fernández-Nieves A, Link D, Weitz D, *Applied Phys. Lett.*, 2003; 82:2610-2612.
38. Wang Y et al., *Nature*, 2012; 491:51-55.
39. Manoharan V, Elsesser M, Pine D, *Science*, 2003; 301:483-487.
40. Cölfen H, Antonietti M, *Angew. Chem. Intern. Ed.*, 2005; 44:5576-5591.
41. Cölfen H, Mann S, *Angew. Chem. Intern. Ed.*, 2003; 42:2350-2365.
42. Studart A, Shum H, Weitz D, *J. Phys. Chem. B*, 2009; 113:3914-3919.
43. Denkov N, Tcholakova S, Lesov I, Cholakova D, Smoukov SK, *Nature*, 2015; 528:392-395.
44. Sirota E, King H, Singer D, Shao H, *J. Chem. Phys.*, 1993; 98:5809-5824.
45. Website of National Institute of Standards and Technology of the United States: <http://wt-pro.nist.gov/wtt-pro>.
46. Thomas A, 2000. *Fats and Fatty Oils*. Ullmann's Encyclopedia of Industrial Chemistry.
47. Kandori K. Gaonkar A (editor), *Applications of microporous glass membranes: membrane emulsification*. In: *Food Processing: Recent Developments*, Elsevier; 1995; 113-142.
48. Christov N, Ganchev D, Vassileva N, Denkov N, Danov K, Kralchevsky P, *Colloids Surf. A*, 2002; 209:83-104.
49. Newton R, Haffegge J, Ho M, *J. Microsc.*, 1995; 180:127-130.
50. Holmberg K, *Handbook of applied surface and colloid chemistry*. Vol. 2 Ch. 16 Identification of lyotropic liquid crystalline mesophases, John Wiley & Sons; 299-332.
51. Bird RB, Stewart WE, Lightfoot EN, *Transport Phenomena* 2nd ed. 2002, Example 12.1-2, Wiley, NY; 376-378.
52. Alexandrov N, Marinova K, Gurkov T, Danov K, Kralchevsky P, Stoyanov S, Blijdenstein T, Arnaudov L, Pelan E, Lips A, *J. Colloid Interface Sci.*, 2012; 376:296-306.
53. Wu X, Ocko B, Sirota E, Sinha S, Deutsch M, Cao B, Kim M, *Science*, 1993; 261:1018-1021.
54. Ocko B, Wu X, Sirota E, Sinha S, Gang O, Deutsch M, *Phys. Rev. E*, 1997; 55:3164-3182.
55. Guttman S, Sapir Z, Schultz M, Butenko A, Ocko B, Deutsch M, Sloutskin E, *PNAS*, 2016; 113:493-496.
56. Gang O, Wu X, Ocko B, Sirota E, Deutsch M, *Phys. Rev. E*, 1998; 58:6086-6100.
57. Gang H, Gang O, Shao H, Wu X, Patel J, Hsu C, Deutsch M, Ocko B, Sirota E, *J. Phys. Chem. B*, 1998; 102:2754-2758.
58. Sirota E, Herhold A, Varma-Nair V, *J. Chem. Phys.*, 2000; 113:8225-8236.
59. Chapman D, *Chem. Rev.*, 1962; 62:433-456.
60. Shalaev E, Zograf G, The concept of 'structure' in amorphous solids from the perspective of the pharmaceutical sciences, *Amorphous Food and Pharmaceutical Systems*, Vol. 281, The Royal Society of Chemistry: Cambridge; 2002, pp.11-30.
61. Bunjes H, Steiniger F, Richter W, *Langmuir*, 2007; 23:4005-4011.

62. Kurklu A, *Renewable Energy*, 1998; 13:89-103.
63. Choi M, Cho K, *Int. J. Heat Mass Transfer*, 2000; 43:209-218.
64. Cho K, Choi S, *Int. J. Heat Mass Transfer*, 2000; 43:3183-3196.
65. Israelachvili JN. *Intermolecular and Surface Forces*. 2011; Academic Press: Amsterdam.
66. Evans EA, Skalak R. *Mechanics and thermodynamics of biomembranes*. 1980; Boca Raton, Fla: CRC press.
67. Wittebrood, M. M., Luijendijk, D. H., Stallinga, S., Rasing, Th., Musevic, I. *Phys. Rev. E*, 1996; 54:5232-5234.
68. Miyano, K. *J. Chem. Phys.*, 1979; 71:4108-4111.
69. Small DM, *The Physical Chemistry of Lipids. From Alkanes to Phospholipids*, Plenum: New York; 1986.
70. Sirota EB, Singer DM. *J. Chem. Phys.*, 1994; 101:10873-10882.
71. Sirota E, Herhold A, *Science*, 1999; 283:529-532.
72. Ueno S, Hamada Y, Sato K, *Cryst. Growth Des.*, 2003; 3:935-939.
73. Sirota E, *Langmuir*, 1998; 14:3133-3136.
74. Lei Q, Bain C, *Phys. Rev. Lett.*, 2004; 92:176103-1 – 176103-4.
75. Sedev R, *Langmuir*, 2001; 17:562-564.
76. Pugh A, *An Introduction to Tensegrity*; University of California Press; 1976.
77. Shinohara Y, Takamizawa T, Ueno S, Sato K, Kobayashi I, Nakajima M, Amemiya Y, *Cryst. Growth Des.*, 2008; 8:3123-3126.

Figure captions

Figure 1. (A) Schematic presentation of the cooling chamber, made of aluminum, with cut optical windows, used for microscope observation of the emulsion samples. (B) The emulsions studied were contained in glass capillaries with rectangular cross-section, placed in the thermostatic chamber and observed through the optical windows [43].

Figure 2. Sample images, used in the study of the kinetics of drop shape evolution. The white lines or curves represent the measured “length” of the drop in a given moment of the experiment. As a measure of drop deformation, we use the aspect ratio $AR = \text{length}/d_{\text{ini}}$. Scale bars, 20 μm .

Figure 3. General evolution scheme for the drop-shape transformations upon cooling of micrometer sized hydrocarbon drops, dispersed in surfactant solutions, as observed with linear alkanes. The scheme is adapted from ref. [43] and expanded by including new information from the current study. Rotator phase R_{Cl} forms on the edges of the geometric shapes in the first stage of the evolution. In the second stage, rotator phase R_{CV} forms very thin (sub-micron) fibres from the corners of larger structures, see text for further explanations.

Figure 4. Images of ensembles of several drop shapes, captured along the evolution process shown in **Figure 3**. (A) Hexagonal platelets; (B) Parallelograms; (C) Bacteria-like droplets with long tails; (D) Fluid rods in coexistence with frozen parallelograms of toroidal topology. The drops in (A), (B) and (D) are from hexadecane, whereas the drops in (C) are from pentadecane. The surfactant used in (A) is $\text{C}_{16}\text{SorbEO}_{20}$, in (B) and (D) $\text{C}_{18}\text{SorbEO}_{20}$, and in (C) $\text{C}_{16}\text{EO}_{20}$. Scale bars, 50 μm .

Figure 5. Panel of images of self-shaped deformed drops from organic liquids with different molecular structures. (A) 1-heptadecene; (B) 1-eicosene; (C) pentadecylcyclohexane; (D) tri-tetradecylglyceride; (E) 1-decanol. The drops from (A-D) are dispersed in solution of $\text{C}_{18}\text{SorbEO}_{20}$ nonionic surfactant, (E) in nonionic $\text{C}_{18}\text{EO}_{20}$. Scale bars, 10 μm .

Figure 6. Pictures of solid particles obtained with different combinations of oils and surfactants: (A) $\text{C}_{20}/\text{C}_{16}\text{EO}_{20}$, (B) $\text{C}_{16}/\text{C}_{16}\text{SorbEO}_{20}$, (C) $\text{C}_{16}/\text{C}_{16}\text{EO}_{20}$. Scale bars, 50 μm .

Figure 7. (A) Evolution of C_{14} (green squares), C_{16} (red circles) and C_{17} (blue triangles) drops with $d_{\text{ini}} \approx 31 \mu\text{m}$ in $\text{C}_{16}\text{EO}_{20}$ solution, at a cooling rate of 0.43 K/min. (B) Pictures of frozen particles of C_{16} and C_{17} , and two images (at lower and higher magnification, respectively) of a C_{14} drop, discharging thin long threads. Note the sharp conical tips on the drop surface from which the threads are extruded. Scale bars, 20 μm .

Figure 8. (A) Typical pictures from the moment just before final freezing of hexadecane droplets, stabilized with $\text{C}_{16}\text{EO}_{20}$ surfactant, for initial drop diameter, $d_{\text{ini}} \approx 31 \mu\text{m}$. The experiments are carried out at different cooling rates, as indicated on the pictures. (B) Pictures of the respective frozen particles, obtained from the droplets shown in (A). Scale bars, 50 μm .

Figure 9. Evolution of the shape of C_{16} drops ($d_{\text{ini}} \approx 31 \mu\text{m}$) in aqueous solution of $\text{C}_{16}\text{EO}_{20}$. (A) Drop length, as a function of time of drop deformation. (B) Aspect ratio as a function of time. (C) Aspect ratio as a function of the sample temperature. Moment $t = 0$ corresponds to the first drop-shape transformation detected. The last (larger in size) points in the respective curves represent the drop deformation just before drop freezing.

Figure 10. (A) Deformations of droplets of C16 in C₁₈SorbEO₂₀ solution, cooled at a cooling rate of 0.44 K/min. The drops have different initial drop size, as shown on the curves. (B) Deformations of C16 droplets in C₁₈SorbEO₂₀ solution, but at a cooling rate of 0.16 K/min. The inset microscope images show deformed drops of different initial diameter, d_{ini} .

Figure 11. (A) Comparison of the individual droplet deformations, achieved from two monodisperse emulsions with drop diameter $d_{ini} \approx 31 \pm 3 \mu\text{m}$, stabilized by C₁₆SorbEO₂₀ and C₁₆EO₂₀, as a function of the sample temperature. Cooling rate is 0.16 K/min. (B) Final aspect ratio in the moment just before drop freezing, for droplets with diameter $d_{ini} \approx 31 \pm 3 \mu\text{m}$, which are cooled at different cooling rates and stabilized by various surfactants.

Figure 12. Images of (A, C) fluid and (B,D) frozen hexadecane droplets, stabilized by two different surfactants, both with well visible frames of cylindrical rods along the edges of the hexagons, stabilized by (A,B) C₁₆SorbEO₂₀ and (C,D) C₁₆EO₂. Scale bars, 20 μm .

Figure 13. Images of flattened torroidal *fluid* drops, with a hole in their central region, stabilized by (A) C₁₆SorbEO₂₀ and (B) C₁₆EO₂. These holes confirm the liquid nature of the interior, the rigid outside frame of the shapes, and are different from the holes that form upon freezing of the shapes into crystals (e.g. Figure 12D). Scale bars, 10 μm .

Figure 14. Schematic presentation of the mechanism of the observed phenomena. (A) Triangular platelet with protruding rods; (B) Cross-section of a rod with an external cylindrical shell of plastic rotator phase (red region) and inner liquid core (yellow region); (C) Cross-section of the platelet body with plastic rotator phase at the platelet periphery (red region) and liquid interior (yellow region); and (D) Interdigitated arrangement of the surfactant molecules (black tails) and alkane molecules (in red) in the surface layer, templating further ordered alkane layers (adapted from ref. [43]).

Figure 15. Schematic presentation of the molecular packing in (A) pseudo-hexagonal rotator phase R_I; (B) orthorhombic solid phase; (C) rotator phase R_V; and (D) triclinic solid phase. All phases are lamellar, with molecules directed perpendicularly (A, B) or tilted (C, D) to the lamellar planes. The molecules in the non-frozen phases (A, C) have some rotational freedom along the longest molecular axis. All these phases were reported for the alkanes in the range studied here, except for the rotator phase R_V which was reported for longer alkanes only (C22-C28), so far.

Figure 16. Energy diagrams for the liquid (L), solid (S) and rotator phases (R) involved in the observed phase transitions, with ΔG denoting the energy difference with respect to the rotator phase R_{CI}. (A) The energy of the rotator phase decreases when it is formed next to a curved interface which makes the cylindrically packed version of the rotator phase R_{CI} more stable than the solid or liquid for temperatures near T_m . (B) From the experimental results one can deduce that two rotator phases are involved in the drop shape transitions, denoted as R_{CI} and R_{CV}. The intersections are approximate and are drawn in a way to allow reproducing the observed phase transitions, which start at different temperatures with the various surfactant types, cf. with Table 4 and Figure 17.

Figure 17. Arrows showing the phase paths upon emulsion cooling, in the presence of stable intermediate rotator phases R_{CI} and R_{CV}, drop deformation starting at temperature T_d , and drop freezing at temperature T_f . (A) Minimum energy path L→R_{CI}→R_{CV}→S, corresponding to drop deformation starting at $T_d > T_m$ and corresponding to surfactants from **group A** in **Table 4**. (B) Evolution path for drop deformation starting at $T_d \approx T_m$ (**group B**). (C) Evolution path for drop

deformation starting at $T_d < T_m$ (**group C**). In (B) and (C) supercooling in the transition $L \rightarrow R_{CI}$ occurs, while the overall sequence of transitions is the same as in (A). (D) direct solidification $L \rightarrow S$ after large supercooling (**group D**).

Figure 18. Energy diagram, illustrating the possibility for formation of a metastable phase, when the barrier to nucleate it is lower, compared to the barrier to nucleate and reach the globally stable state for a given temperature. The case of stable solid and metastable rotator phase is shown here, but similar diagrams may apply for the transitions involving two rotator phases. The barriers are lower for transitions between phases which are structurally similar (e.g. R_I to orthorhombic solid phase or R_V to triclinic solid phase).

Figure 19. Interfacial tension as measured by the pendant drop method, as a function of temperature, for hexadecane drops immersed in the aqueous solutions of two different surfactants, as indicated in the figure. The experimental error in determining the interfacial tension is ± 0.1 mN/m. The vertical dashed line denotes the melting point for hexadecane (T_m), which coincides with the initial droplet deformation temperature for these surfactants ($T_d = T_m \pm 1$ °C, explained also in Table 4).

Tables:

Table 1. Structural formulas of the non-alkane organic phases studied.

Table 2. Properties of the non-alkane organic phases studied (hexadecane is presented for comparison).

Table 3. Properties and structural formulas of the surfactants used (all characteristics are taken from the descriptions provided by the surfactant producers).

Table 4. Groups of surfactants with respect to their effect on the drop “self-shaping” phenomenon for hexadecane (see text for explanations).

Highlights

- 5 classes of molecules, over 60 oil/surfactant combinations exhibiting self-shaping
- The role of surfactant structure packing for templating new phases upon cooling
- Molecular classification of four families of surfactants with corresponding behaviours
- Mechanistic role of a previously unknown second plastic crystal phase
- Coherent explanations of the above effects, based on thermodynamic principles

ACCEPTED MANUSCRIPT